International Journal of Heat and Mass Transfer 154 (2020) 119751

Contents lists available at ScienceDirect

International Journal of Heat and Mass Transfer

journal homepage: www.elsevier.com/locate/hmt

# Raman-based Nanoscale Thermal Transport Characterization: A Critical Review

Shen Xu[a,c,#], Aoran Fan[b,#], Haidong Wang[b], Xing Zhang[b,*], Xinwei Wang[c,*]

[a] School of Mechanical and Automotive Engineering, Shanghai University of Engineering Science, Shanghai, P.R. China
[b] Key Laboratory for Thermal Science and Power Engineering of Ministry of Education, Department of Engineering Mechanics, Tsinghua University, Beijing, P.R. China
[c] Department of Mechanical Engineering, Iowa State University, Ames, Iowa 50011, USA

ARTICLE INFO

*Article history:*
Received 20 December 2019
Revised 18 March 2020
Accepted 5 April 2020

*Keywords:*
Raman spectroscopy
Temperature probing
Laser flash Raman spectroscopy
Energy Transport State-resolved Raman
Micro/nanoscale materials

ABSTRACT

Raman-based thermal characterization is regarded as an invaluable tool in micro/nanoscale heat transfer research, offering exceptional contrast in conjunction with high specificity of noncontact and material specific temperature measurement compared with competing thermometry techniques at the micro/nanoscale. It has been extensively used to determine the thermophysical properties of micro/nanoscale materials. However, for commonly used steady state Raman methods, as two concluded main factors, the temperature coefficients of Raman properties and heating level (or optical absorption) will affect the accuracy of resulting temperature and thermal properties. In this review, we critically discuss the mechanism of Raman spectrum response to temperature and possible error factors in calibration and measurement. In addition, the influence of measurement setup is discussed, and possible technical solutions for improving the measurement accuracy are reviewed. Among noble developments in Raman-based thermal characterizations, the transient heat transfer analysis has been coupled to advances in noncontact Raman-based thermal measurement. By enhancing the temporal and spatial resolution in existing technical conditions, more efficient and accurate transient thermal properties measurement can be realized. Particular attention is paid to the so-called resolved Raman techniques for simultaneous measurement of multiple thermal properties at the micro/nanoscale. In particular, we critically review how these tools can reveal new insights into the complex energy transport processes in 2D semiconductors, which have been impossible to tackle using traditional tools. Considering its precision and sensitivity, there is still a large room for development of Raman techniques for the investigation of complex and coupled heat transfer process in low dimensions and new materials.



## 1. Introduction

### 1.1. Raman spectroscopy background and mechanism

When light irradiates a substance, scatterings will occur. In addition to Rayleigh scatterings (the elastic component) that have the exact same wavelength of the excitation light, there are other components which have longer or shorter wavelengths than that of the excitation light [1,2]. The latter phenomenon was first observed by CV Raman and is thus termed as Raman scattering. Raman scattering is an inelastic scattering between incident photons and molecules or lattices in materials [3]. The scattering mechanism is shown in Fig. 1. When the incident light comes in at a certain frequency, molecules in the substance absorb some photons, jump to higher virtual states, then transit to different energy states, and release the rest energy to surroundings [4]. There are two types of Raman scatterings. The scattered photons that have a lower frequency than the incident one are called Stokes scattering. Anti-stokes scatterings have a higher frequency than the incident light [5]. For the factor that the density of the ground state is higher than that of excited states, the strength of Stokes scattering usually is much stronger than that of anti-Stokes scattering.

Since Raman scatterings are generated in the collision between incident photons and phonons in materials, the change of the frequency, termed Raman shift/frequency/wavenumber in Raman spectrum, is given as the characteristics of materials [6]. The vibration of different kinds of atomic groups is matchless. For a specific atomic group, the frequency of the scattered light is unique. Furthermore, the Raman shift of Raman peaks is mainly related

* Corresponding authors.
*E-mail addresses:* x-zhang@mail.tsinghua.edu.cn (X. Zhang), xwang3@iastate.edu (X. Wang).
# Equal contribution authors.

https://doi.org/10.1016/j.ijheatmasstransfer.2020.119751
0017-9310/

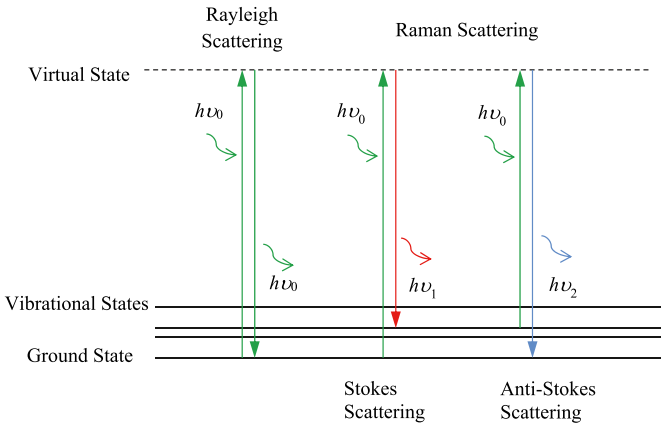


**Fig. 1.** The mechanism of Stokes and anti-Stokes scatterings.

to the internal structure and functional groups in tested materials at room temperature, no matter what the wavelength of the excited laser is. Thus, the resulting Raman spectrum is also called "fingerprint spectrum", and the molecules of the constituent substances can be identified according to their unique Raman shifts. Though the Raman scattering signal is much weaker compared with Rayleigh scattering, which is blocked in the optical system, it has a pretty good signal-noise ratio if the integration time is long enough for scattering accumulation in the detector.

### *1.2. Raman thermometry*

Peaks in a Raman spectrum can characterize lots of features of materials of interests [7]. To be specific, Raman shift could be used to determine the composition of materials, the linewidth of Raman peaks illustrates the lifetime of phonons in materials, and the intensity of Raman peak depends on the population of phonons in materials. Along the advancement of Raman spectroscopy applications, it is found that Raman scattering cannot only be used to characterize chemical structures, but is also related to macroscale physical properties, such as the temperature, stress, and grain size of materials. From the classic physical perspective, when the incident light irradiates the Raman-active bonds, the electromagnetic field of the light will alter its electric dipole oscillation, and the electric dipole moment depends on the electric field intensity of the incident light and its own polarizability. The change in temperature varies the polarizability, which in turn affects the generation of Raman signals. According to this, temperature probing and heat-transfer analysis can be realized based on Raman signals. Thus, using the intrinsic properties of Raman peaks (intensity, linewidth and Raman shift) and corresponding heat transfer models, temperature and thermophysical properties could be determined.

Raman thermometry has very unique advantages of non-contact and micro/nanoscale accessibility in temperature measurement and thermal probing than traditional methods, especially at the micro/nanoscale [5]. In commonly used contact-mode temperature probing methods, like thermocouples and thermal resistors, a temperature probe is needed to attach to the sample's surface, and the temperature is then measured based on the voltages over the resistors. Thermal paste is needed to ensure a good contact between the probe and the sample surface, but it will inevitably cause contamination or damage to the sample to a certain extent [8]. Noncontact optical temperature measurements are preferable and have broader application prospects. On the other hand, as the Micro-Electromechanical Systems (MEMS) continuously advance, the scale of critical temperature distribution is continuously decreasing in micro devices as well as temperature measurement. The scales are too small for the conventional thermal measurement methods to get access for precise and specific temperature measurement. This is particularly true for nanomaterials, such as 2D materials. Alternatively, the excitation laser in the Raman system can be focused to a very small spot with sub-micron size (~500 nm under 100× objective [9]) and thus achieves temperature probing at a very small scale. Besides, one critically important feature of Raman-based temperature probing is material-specific, meaning it does not only measure temperatures, but also tells whose temperature it is based on the material-specific Raman spectrum [8,10,11].

Therefore, Raman-based thermometry has wide applications as an effective temperature-probing method at micro/nanoscale scale. Recently, numbers of novel Raman-based temperature measurement techniques have been developed to meet new demands of the thermal measurement of new nanomaterials and structures. A new concept of laser flash-Raman spectroscopy method was first proposed in July 2014 for conveniently investigating the transient heat transfer process in suspended 2D materials and measuring its thermal diffusivity [12]. The method was developed and validated in the same year for thermal properties measurement of micro/nano wires based on steady state and transient response of Raman spectroscopy [13]. In 2015, the time-domain differential Raman method [14] and frequency-resolved Raman method [15] were established in February and October, respectively, for 1D structure thermal characterization. These two methods eliminated the temperature coefficients calibration of Raman properties and optical properties requirement in data processing. Besides, in the same time, the laser flash-Raman spectroscopy method was further developed for supported 2D materials measurement [16]. In 2017, a significant advancement in Raman thermometry was energy transport state-resolved Raman (ET-Raman) with an emphasis on interface energy transport and the hot carrier diffusion measurement [17-21]. This is, for the first time, hot carriers were studied using Raman spectroscopy and the time resolution was pushed to picoseconds. Based on ET-Raman, frequency-domain energy transport state-resolved Raman (FET-Raman) was developed in 2018 to largely improve the measurement precision [22]. At the same time, along with the development of 2D van der Waals heterostructures, a variable-spot-size laser flash Raman spectroscopy method developed in 2018 enabled thermal and optical measurement of supported 2D van der Waals heterostructures [23]. Aiming to resolve the modulation limit of the heating laser, a dual-wavelength laser flash Raman spectroscopy method has been proposed in 2018 to combine a picosecond laser with the heating laser to realize high temporal resolution for transient thermal measurement [24]. This method was extended to map anisotropic thermal properties of materials in 2019 [25].

Our goal of this review is to provide in-depth comments and discussion on diverse advanced Raman techniques for characterizing heat transfer process in micro/nanomaterials, especially focus on 2D atomic layer materials [26]. Pervious research has shown great achievement in measurement of thermal properties using Raman techniques. However, take few-layered $MoS_2$ as an example, for the same material, the value of measured thermal conductivity ranges from 15 W/(m•K) to 100 W/(m•K) [27-31]. This unexpected fact may be raised either by the difference in the intrinsic structure of the tested sample from one to another, or by the interaction of the sample at the interface with substrates when it is supported. Additionally, a preferred reason in this perspective is errors in measurement. Therefore, in this review, some focus is given on the physical mechanism of different Raman techniques, possible sources of measurement errors, and advanced measures to reduce or avoid the errors. Section 2 comprehensively introduces the temperature responses of materials in Raman spectrums, the unique advantages of Raman temperature measurement, and the develop-

ment of high spatial resolution Raman measurement. The critical factors of Raman temperature measurement and the temperature coefficient calibration are also discussed in Section 2. The steady-state Raman-based characterization and the corresponding heating level evaluation are discussed in Section 3. In Section 4, new advancement is reviewed in temporal Raman-based characterization. Section 5 introduces the recent new applications of the combination of steady-state and ultrafast Raman spectrum in complex heat transfer process investigations. Finally, a summary in the accomplishment and future work is given in Section 6.

## 2. Raman-based Temperature Measurement: Principle, Feature and Uncertainties

### 2.1. Temperature response of Raman properties: accuracies and errors

In a Raman spectrum, all properties of Raman peaks (intensity, Raman shift, and linewidth) are observed in response to temperature variations [8,32,33]. They are tightly related to the intrinsic molecular structure, which is directly affected by temperature, so they can be used as temperature indicators for temperature probing. Generally, when temperature rises, the Stokes Raman shift of a feature peak is red-shifting, the linewidth is broadening, and the peak intensity is decreasing. When the temperature variation range is not very large (e.g. ~100 °C), the change of the Raman shift, linewidth, and intensity of Raman peaks shows a linear relation against temperature, so this relation could be utilized to quickly determine the temperature of tested samples.

#### 2.1.1. Raman shift-based temperature measurement

The Raman shift of feature peaks originates from dipoles in chemical structures in lattice of materials. Since the lattice spacing will vary with temperature variation, the shift of Raman scatterings shifts against temperature. For most materials, Raman shifts of feature peaks will shift to a lower value when temperature goes higher. Both Stokes and anti-Stokes signals will shift simultaneously, however, the former one is much stronger and is more easily recognized as a steady and accurate signal for temperature measurement. Variation of Stokes signal shift by temperature can be expressed using the following equation [34].

$$\omega(T) = \omega_0 + A\left(1 + \frac{2}{e^{\frac{h\omega_0}{4\pi kT}} - 1}\right) + B\left(1 + \frac{3}{e^{\frac{h\omega_0}{4\pi kT}} - 1} + \frac{3}{\left(e^{\frac{h\omega_0}{4\pi kT}} - 1\right)^2}\right), \tag{1}$$

where $\omega$ is the shift/frequency of a specific Raman peak, $h$ the Planck constant, $k$ the Boltzmann constant, and $T$ the absolute temperature of the sample. $\omega_0$ is the Raman frequency at room temperature, and $A$ and $B$ are constants specific to materials. The shift of Raman peaks is sensitive to temperature variation and easy to observe and define in the spectrum. It is the most widely-used property for Raman-based temperature measurement. However, temperature gradient-induced stress in materials will shift the Raman frequency (discussed later in this section) and consequently affect the accuracy of the results in Raman shift-based temperature measurement. When the temperature rise is not very high, the stress effect will be very weak and could be neglected. The Raman shift could still be an accurate temperature probe.

#### 2.1.2. Raman linewidth-based temperature measurement

Another intrinsic property of a Raman peak is its linewidth. It depends on the lifetime of optical phonons in the process of Raman signals generation. When temperature changes, the lifetime of phonons changes and the linewidth of the Raman peak is consequently changed. Generally, the linewidth of Raman peaks broadens when temperature rises. The relation between temperature and linewidth can be mathematically depicted as [34].

$$\Gamma(T) = C\left(1 + \frac{2}{e^{\frac{h\omega_0}{4\pi kT}} - 1}\right) + D\left(1 + \frac{3}{e^{\frac{h\omega_0}{4\pi kT}} - 1} + \frac{3}{\left(e^{\frac{h\omega_0}{4\pi kT}} - 1\right)^2}\right). \tag{2}$$

$\Gamma$ is the Raman peak linewidth. Analogously to Eq. (1), $C$ and $D$ are the constants depending on materials. However, the linewidth is less used for temperature determination in the practical thermal measurement due to its less sensitivity to temperature. Obtaining the good linewidth information requires a sound Raman signal. Otherwise a large error may be induced in the measured temperature. Contrast to the shift of Raman peaks, the linewidth is least affected by stress, and could be used as an alternative temperature probe when large stress exists in materials.

#### 2.1.3. Intensity-based temperature measurement

Raman scatterings originate from the inelastic scattering of photon-atom collision. At different temperatures, the density of atoms in diverse excited states is different, so the measured Raman intensity changes with temperature under the same incident light source and the same acquisition time. Because of the difference in the mechanism of Stokes and anti-Stokes scattering, the two tend to have opposite trends in intensity change along temperature change. Under the same excitation and integration conditions, the Stokes peak intensity decreases as temperature increases while the anti-Stokes peak intensity increases. Take silicon as an example, the ratio of the two scatterings has the expression as Eq. (3) [34].

$$\frac{I_s}{I_{as}} = \frac{\alpha_i + \alpha_{as}}{\alpha_i + \alpha_{as}}\left(\frac{\omega_i - \omega_R}{\omega_i + \omega_R}\right)^4 \exp\left(\frac{h\omega_R}{2\pi kT}\right), \tag{3}$$

where $\alpha_i$, $\alpha_s$, $\alpha_{as}$ are the absorbance of the material at the incident light frequency, the Stokes frequency and the anti-Stokes frequency, respectively. $\omega_R$ is the frequency of the Raman peak; $\omega_i$ is the incident light frequency. From Eq. (3), it is clear that the ratio of the Stokes scattering intensity to anti-Stokes scattering is a function of the absolute temperature in the unit of K. This feature can be directly used for temperature determination. However, for many commercial Raman spectroscopies, anti-Stocks scatterings could not be measured simultaneously with the Stocks scatterings, as its frequency is higher than the incident laser and is out of the available range of Raman systems. Also, anti-Stocks scatterings are much weaker than Stocks scatterings, which reduces the accuracy of the intensity-ratio based method in practical temperature measurement. Instead, the intensity of Stocks scattering is often used individually for temperature measurement.

### 2.2. Material specific temperature measurement: the great feature of Raman

Generally speaking, all structure related spectroscopy techniques could be applied to measure temperature, such as florescence methods and Fourier-transform infrared spectroscopy (FTIR), etc. Florescence methods can be used to detect a single macromolecule [35,36] and probe temperature with a high sensitivity [37,38]. Zhou, *et al.* developed a convenient method to produce a poly(dimethylsiloxane) (PDMS)-ZnO quantum dots (QDs) composite film for the whole chip temperature measurement and a very high sensitivity of the QDs fluorescence to temperature was obtained to be 0.4 nm/°C [37]. However, the drawback of the florescence method for temperature measurement is that the peak in florescence spectrum is very broad and it is not material specific. When there is more than one molecule radiating florescence signals, the overlapped peaks are hardly discrete.

Compared with the fluorescence method, highly structure-distinguished characterization is one of the most promising features of Raman spectroscopy [39,40]. That means the spatial resolution of its temperature measurement is not simply determined by the optical focal spot, but by the material size. Also, the Raman scattering based temperature measurement is material-specific, meaning the Raman peak can used to distinguish and measure the temperature of a specific material if several materials stack together. For instance, when a 2D material is patterned to a size smaller than the laser focal spot, still we can obtain the Raman signal from that material and measure its temperature. Also for an interface, when two materials are immediately next to each other, Raman thermometry can provide the temperatures of both materials, such as a layer graphene on SiC [10]. In Tang's work, as a few-layered graphene is thin enough ($\sim$ nanometers thick), the excitation laser can easily penetrate the graphene layer and irradiate the surface of substrate. As a result, two featured Raman peaks were obtained simultaneously in one Raman spectrum: one for graphene, and one for SiC. The temperature difference $\Delta T$ between these two materials can be immediately determined in accordance with their Raman temperature coefficients. With the knowledge of the local laser heating level $q$, the interface thermal resistance can be calculated using $R_{tc} = \Delta T/q$ [8,10,11].

It is important to note that the measured temperature of substrate is not the one directly at its surface, but rather an intensity-weighted temperature [18] over a finite volume. This includes two major contributions. First, it is an averaged temperature in the substrate across the focal depth [11]. The skin depth of incident laser is $\tau = \lambda/(4\pi k)$, where $\lambda$ is the wavelength of the laser and $k$ the extinction coefficient of the substrate. Then the average temperature across $\tau$ could be calculated as $\int_0^\infty Te^{(-x/(\tau/2))}dx/\int_0^\infty e^{(-x/(\tau/2))}dx$, which approximates the temperature value at $x = \tau/2$. Take silicon substrate as an example, its skin depth $\tau$ equals 820 nm when the incident wavelength is 532 nm. Thus, the measured temperature of Si substrate equals the value at 410 nm away from its surface in Raman thermometry using a 532 nm laser. Second, the measured temperature is further averaged over the irradiated area [18] in the lateral direction. The energy of incident laser has a Gaussian spatial distribution at the focal spot on the sample's surface, and the resulting Raman scattering will be non-uniform and also have a Gaussian distribution. To fully consider this spatial effect, a Raman-intensity weighted average temperature has been proposed for temperature determination. It has the expression as $\Delta\bar{T} = \iiint \Delta T I_{Raman}dV/\iiint I_{Raman}dV$.

Numerical modeling is a powerful way to precisely determining the interface thermal conductance based on the measured temperatures. A 3D numerical modeling could be conducted to simulate the Raman intensity-weighted temperature [18]. In Yuan's recent work, a 3D theoretical model was developed to depict the heat transfer in a $MoS_2$ layer and the substrate bulk, and across the interface in a Raman-based experimental study. In the experiment, Raman scatterings of $MoS_2$ and the substrate were measured at two designed thermal steady-states: Raman excitation laser was focused under 20$\times$ and 100$\times$ objectives to generate two different heating spots. The modeling in accordance with the experiment used two governing equations to describe the heat conduction in $MoS_2$ and the substrate, respectively, and the interface heat conduction. Under a large heating spot, the upper figure in Fig. 2(d), the in-plane heat transfer is less important. The thermal energy transported primarily across the interface and contributed to the temperature rise in the substrate. In this case, the interface thermal resistance is the main factor affecting the steady-state temperature rise in both $MoS_2$ and the substrate.

In contrast, the in-plane heat transfer becomes more significant when the heating spot is extremely small in the second case [lower figure shown in Fig. 2(d)]. The in-plane thermal conductivity of $MoS_2$ dominated the overall heat transfer process and determined the temperature rise. Initial values were given for the electron diffusion coefficient $D$, the parameter related to in-plane heat transfer in $MoS_2$, and interface thermal resistance $R$, and substituted in the equations to simulate the temperature rise in $MoS_2$ and substrate. Then the modeling result was compared with the experimental results in Raman-based thermal measurement to find out $D$ and $R$ [17,18]. As shown in Fig. 2(a) and 2(b), pairs of $D$ and $R$ were found for 20$\times$ and for 100$\times$, respectively. The crossover point would indicate the real $D$ and $R$ for the tested sample as shown in Fig. 2(c).

### 2.3. Higher spatial resolution of Raman thermometry: material control and optical field control

#### 2.3.1. Material determined temperature resolution

The temperature measurement based on Raman spectrum can be done by evaluating the Raman anti-Stokes/Stokes ratio [41-43], the full linewidth at half maximum of Raman peaks [44-46], or the red-shift of characteristic Raman wavenumber [34,46,47]. The spatial resolution of temperature measurement is limited by the size of focused laser spot if the sample's size is larger than the laser spot size. By using an objective lens with a high numerical aperture (NA), the diameter of optical focal spot can be close to or smaller than 1 $\mu$m. However, as mentioned above, the spatial resolution of temperature measurement can be further increased to the nanometer level if the size of tested sample is at nanoscale, such as carbon nanotubes (CNT), nanowires, nanoribbons, etc.

Besides this strategy for nanoscale temperature measurement, another way to breaking through the diffraction limit of a laser spot is to use near-field Raman spectroscopy, e.g. surface-enhanced or tip-enhanced Raman spectroscopy [48], for probing temperature in extremely small areas. The intensity of near-field Raman signal can be significantly enhanced by a factor ranging from $10^3$ to $10^6$ or even higher [49-52]. Yue *et al.* conducted noncontact sub-10 nm temperature measurement using tip-enhanced Raman method [48]. The incident Raman laser was focused by an AFM tip into a hemisphere with a diameter less than 10 nm in a silicon substrate. With the help of electric field enhancement near the tip, Raman scatterings from the substrate could be detected for temperature measurement, while the scatterings from such a small area would be too weak to measure in regular Raman thermometry. Tang *et al.* used the microparticles and microfiber to introduce near-field heating, and has achieved far-field simultaneous temperature and stress mapping with a resolution of 20 nm in the substrate [53]. With the help of featured Raman peaks and near-field laser ultra-focusing, it could be possible for us to measure the temperature of a single molecule or nanoparticle.

#### 2.3.2. Spatial resolution in surface-enhanced Raman

Maher *et al.* studied the temperature dependence of Raman anti-Stokes/Stokes ratio in the case of surface-enhanced Raman spectroscopy (SERS) [54]. 514 and 633 nm wavelength laser beams were used as different excitation sources on dried Ag colloids. The result shows that the anti-Stokes/Stokes ratio has clear temperature dependence under the surface-enhanced Raman scattering conditions. Such temperature dependence either comes from the direct laser heating of molecules or vibrational pumping via SERS processes, or a combination of both. Further analysis demonstrates that these two effects can be distinguished by temperature scanning guided by a comprehensive model considering the effective mode temperature and SERS enhancement factor due to the electromagnetic and chemical interactions. Pozzi *et al.* studied the Stokes and anti-Stokes SERS down to single molecule level and found its correlation with local heating [55]. Higher excitation power increases local temperature of single molecule and increases

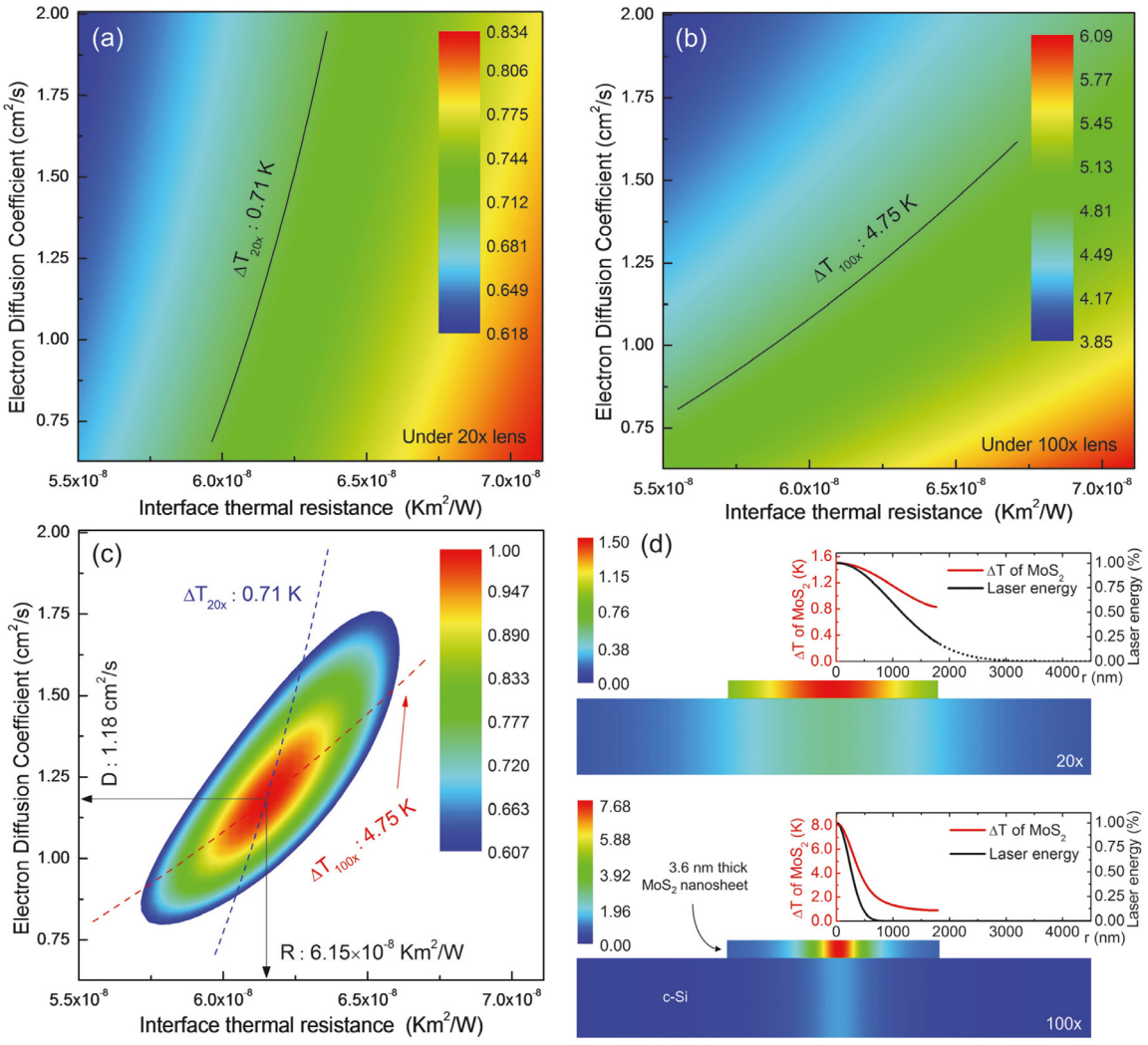


**Fig. 2.** 3D numerical modeling for 3.6 nm thick $MoS_2$ sample on c-Si substrate. The temperature against the electron diffusion coefficient and interface thermal resistance under 20× objective (a) and under 100× objective (b). (c) Determined *D* and *R* as well as the uncertainty region. (d) Theoretical temperature rise distribution in the sample under laser heating with 20× and 100× objective lenses using the determined *D* and *R* for this sample. (Reprinted from Ref. [18]. Reproduced with permission of The Royal Society of Chemistry. All rights reserved)

its diffusion from the hot spots. The local heating effect will increase or decrease the anti-Stokes/Stokes ratio and SERS intensity simultaneously, depending on the geometry of the given aggregate. However, confident temperature calculation was unlikely due to the large uncertainty in the wavelength dependence of enhancement factor, which was highly relevant to the location of the molecule. The author suggested that more accurate temperature determination can be done by utilizing chemisorbed or anchored molecules that can eliminate the variations caused by molecular diffusion, or by utilizing molecules with prominent modes at terahertz Raman shift where the difference caused by different wavelength dependent detection efficiencies becomes negligible as the difference between the anti-Stokes and Stokes frequencies approaches zero.

### 2.3.3. Molecular level temperature resolution in tip-enhanced Raman

Balois *et al.* measured the local temperature of a single-walled CNT (SWCNT) by using tip-enhanced Raman spectroscopy (TERS) [56]. Similar to the temperature measurement from SERS, the local temperature of CNT can be detected by measuring the anti-Stokes/Stokes ratio according to the Boltzmann distribution function under the tip-enhanced Raman scattering conditions. The radial breathing mode (RBM) was chosen for TERS measurement in this study, because of the small wavelength gap (10 nm) between the anti-Stokes and Stokes frequencies. The result indicates that the smaller gap distance between CNT and tip causes higher enhancement factor and higher temperature rise. In comparison with SERS, TERS turns out to be a better choice for temperature measurement at the nanoscale since the location of molecules can be precisely known, reducing the uncertainty caused by the molecular diffusion under laser heating. Park *et al.* investigated the temperature dependent TERS of malachite green on gold substrate and confirmed its feasibility in molecular temperature measurement and single molecule dynamics [57].

Fig. 3 shows the temperature dependent TERS spectra of malachite green. It is seen that the linewidth of characteristic Raman peaks is broadened with increased temperature due to the enhanced thermally activated modes. The broadened linewidth follows an Arrhenius behavior with tunable coupling strength and lifetime of exchange modes, as illustrated in Fig. 4. It was found in the experiment that the center frequencies of TERS spectra were scattered as temperature increased, unlike the continuously red-shifted Raman wavenumber measured in micro-Raman method.

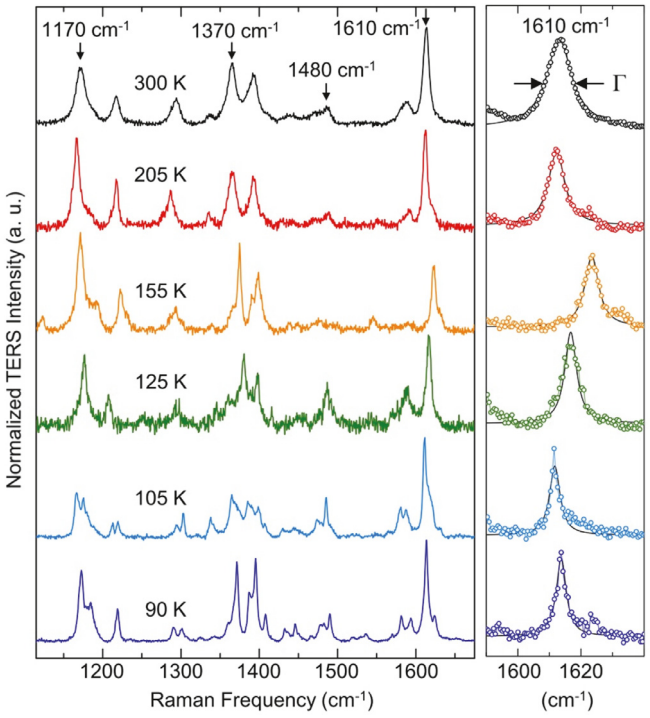


**Fig. 3.** Temperature dependent TERS spectra of malachite green. The linewidths of characteristic Raman peaks increase as temperature increases, while the center wavenumber shift shows no positive correlation with the temperature change. (Reprinted with permission from Ref. [57]. Copyright (2016) American Chemical Society)

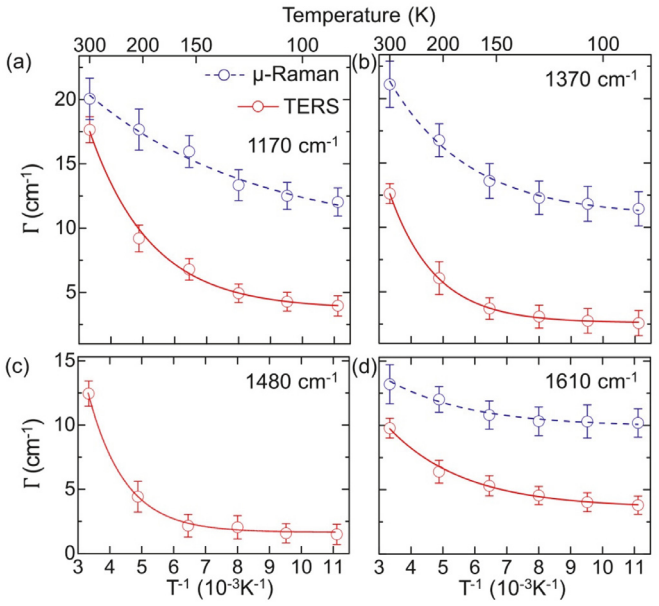


**Fig. 4.** Temperature dependent TERS linewidths at different modes, including C-H in-plain bends (1170 $cm^{-1}$) and twists (1370 $cm^{-1}$), bending of the methyl group (1480 $cm^{-1}$) and N-C stretching mode (1610 $cm^{-1}$). The broadened line linewidth from micro-Raman measurement is shown for comparison. The solid line is given by doing Lorentzian line fit analysis. (Reprinted with permission from Ref. [57]. Copyright (2016) American Chemical Society)

This is due to the inhomogeneous molecules tested in different TERS measurements.

The result shown in Fig. 4 demonstrates the feasibility of detecting the local temperature of a few molecules within TERS probing volume. The micro-Raman method captures signal from the ensemble average over $\sim 4\times10^5$ molecules, while the TERS spectra show signal emerges only from average 1∼2 molecules. As a result, the line shape of micro-Raman peak is significantly broader and the temperature sensitivity is much limited.

### *2.4. Critical factors inducing large errors in Raman temperature measurement*

Although each of three properties of Raman peaks can be used for temperature probing, they have different sensitivities to temperature. The linewidth of Raman peaks has the weakest response but mainly depends on temperature. The Raman frequency has a relatively stronger sensitivity to temperature rise, but the thermal stress raised in the measurement will lower the accuracy of shift in temperature response. The intensity has a very strong sensitivity, but is significantly affected by optical focusing, and thus requires very carefully defined focus and control during the measurement. Among these three properties, the Raman shift is most widely used to measure temperature. Before using Raman-based temperature measurement, several issues of the experimental setup should be carefully addressed.

#### *2.4.1. Stress*

In Raman spectroscopy, the Raman excitation laser is focused to a spot on a surface. The temperature distribution is inevitably uneven. It induces a temperature gradient in the sample and thus thermal stress is generated. Different types of stress in the sample will produce the opposite shifts in the shift of Raman peaks. If the stress is tensile stress, a negative shift in Raman wavenumber will appear in Raman spectrum, while a positive shift indicates a compressive stress [58-60]. Errors may exist in the Raman wavenumber-based temperature measurement when the stress effect in the material is non-negligible. On the other hand, the Raman peak linewidth has weak dependence on stress. Beechem *et al.* [61] reviewed the theory of temperature and mechanical response in Raman spectrum, and further conducted the experimental study in doped polysilicon microheaters. Their calibration results show that the wavenumber has a linear relation against both temperature and stress. The linewidth shows a parabolic fit against temperature over the temperature range from 0 °C to 600 °C, but it is insensitive to stress in the same temperature range. It can provide a more accurate result in this situation in comparison with wavenumber-based method. This offers a possible way for studying the thermal stress in the sample using both wavenumber-based and linewidth-based methods. In utilization of the distinct response of Raman peak linewidth and wavenumber, Tang *et al.* studied the conjugated temperature and stress distribution in a silicon wafer under microscale glass particles and fibers [9]. Tang's work shows that the stress-induced Raman shift is about $10^{-1}$ order of the temperature-induced Raman shift. If the temperature rise is not very high, the stress effect can be neglected.

#### *2.4.2. Optical focusing*

Another issue in Raman-based thermal characterization is optical focusing. The quality of Raman peaks as well as their intrinsic properties is in fact very sensitive to the optical focusing level, though this effect has not been studied a lot or neglected in the past. Xu *et al.* has studied this effect in detail using a 100× microscope objective on silicon wafers' surface [62]. Fig. 5 shows that Raman intensity ($I$), linewidth ($\Gamma$), and shift ($\omega$) of Silicon's 521 $cm^{-1}$ peak vary with the focal level in the vertical direction. The intensity is increasing, the linewidth is narrowing, and the shift is increasing as the tested surface is approaching the focal point. Also the maximum intensity, Raman shift and the minimum linewidth arise at the well-focused level simultaneously (the red dash line

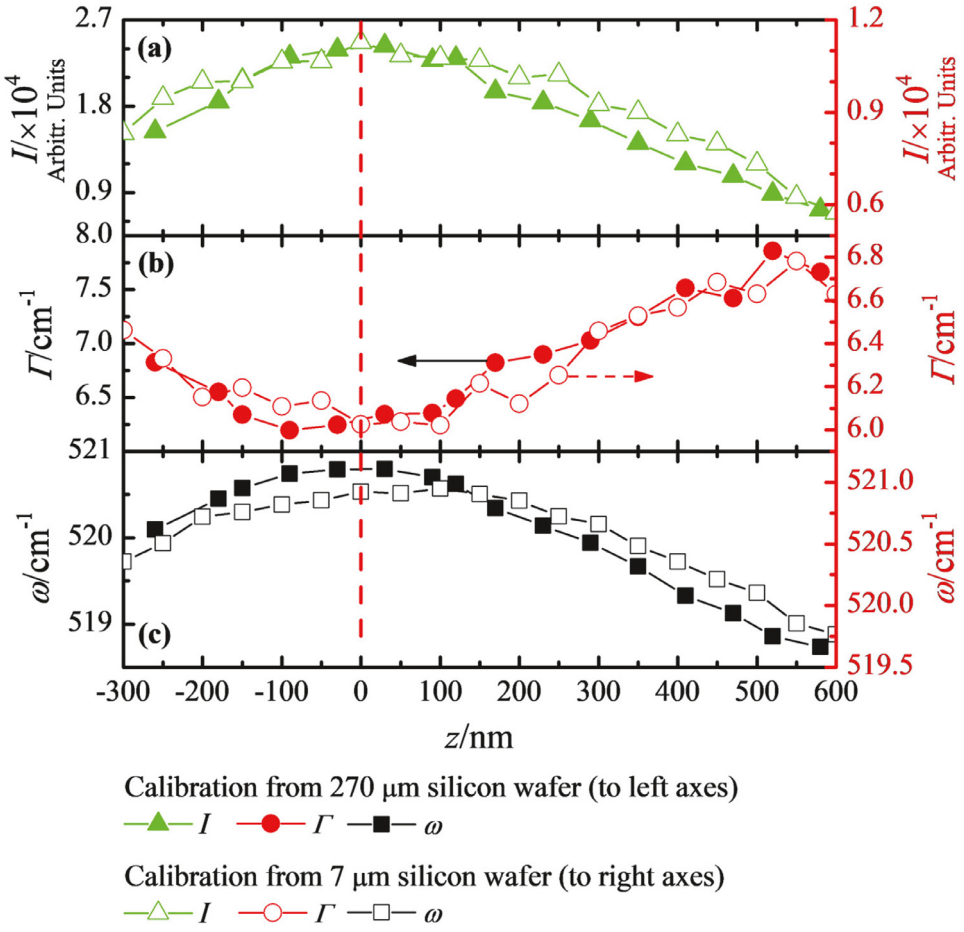


**Fig. 5.** Out of focusing effect on the deviation of the Raman spectrum at different focal levels on single crystalline silicon wafers. (a) Peak intensity ($I$), (b) linewidth ($\Gamma$), and (c) 521 $cm^{-1}$ peak shift ($\omega$). (Reprinted from Ref. [62]. Reproduced with permission of John Wiley & Sons, Ltd. All rights reserved)

in Fig. 5) [63]. Among these three properties, the Raman intensity is most sensitive to the focal level. When the focusing level is changed by up to 600 nm, the intensity is reduced by ~37.5%, while the linewidth is increased by 16% and the wavenumber only shifts by ~1 $cm^{-1}$.

Fig. 5 also shows that under a 100× objective, the variation in Raman spectra is negligible when a tiny stage shift of 200 nm occurs around the focal level in the $z$ direction. Thus, the focusing issue is less critical in a fast measurement of several seconds. It becomes more noteworthy in a longer integration time. Well maintaining the tested surface at a highly controlled focusing level becomes a key issue in Raman-based temperature measurement.

Several reasons identified in previous work would cause the shift of tested samples away from the focal level. As in Raman scattering-temperature calibration, a heating stage was generally applied. Though the thermal expansion of film-like samples, such as 2D materials, is negligible, thermal expansion from the sample stage and supports is large during the heating process. They are the main reasons for shifting the focal level. Great efforts have been made in previous work to reduce this effect [9,63]. A surface image with laser spot at well focused level was used as a criterion. After the sample shifted, the stage would be adjusted again to match the reference image. Another reason causing the focal level's shift is the backlash of the sample stage due to the mechanical stress and the gravitational force. To reduce this effect, several technical methods have been employed in Wang's lab. A tiny over-adjustment was applied to the stage before the stage was locked. Then the stage is allowed to stay there in stationary state for a while to remove the extra mechanical stress and reach the equilibrium level. Recently an auto-focusing stage was developed in Wang's lab to maintain the surface at the focused level [17,18,21]. A self-developed system controlled the movement of the sample stage in the $z$ direction with a minimum single step of ~5 nm. It moved the stage upward step by step, and the Raman spectrum of the surface was recorded in each step. Simultaneously, the control system would analyze the obtained Raman spectrums, define the position with the highest intensity that indicates the best focusing level, and send back the position information to the stage. Using this auto-focusing technique, no matter how much the stage thermally expands, the sample surface would be always best focused in the Raman system.

### 2.4.3. Interface optical interference

In Raman-based temperature measurement, the effect of interface optical interference is brought up in measurement of supported nanomaterials. Upon laser heating, a tiny spacing appears between the nanomaterial and its substrate because of the different thermal expansion coefficients of two materials, or some interface spacing exists due to sample preparation. The incident laser and Raman scatterings reflect multiple times at the two surfaces of the interface, and induce very strong optical interference. It increases the incident laser absorption and enhances the Raman intensity significantly [10,11,64]. Work by Tang *et al.* first reported a nanoscale rough contact between chemical vapor deposition (CVD) graphene and substrate [65], as shown in Fig. 6. The studied graphene/Si interface was found to contact with each

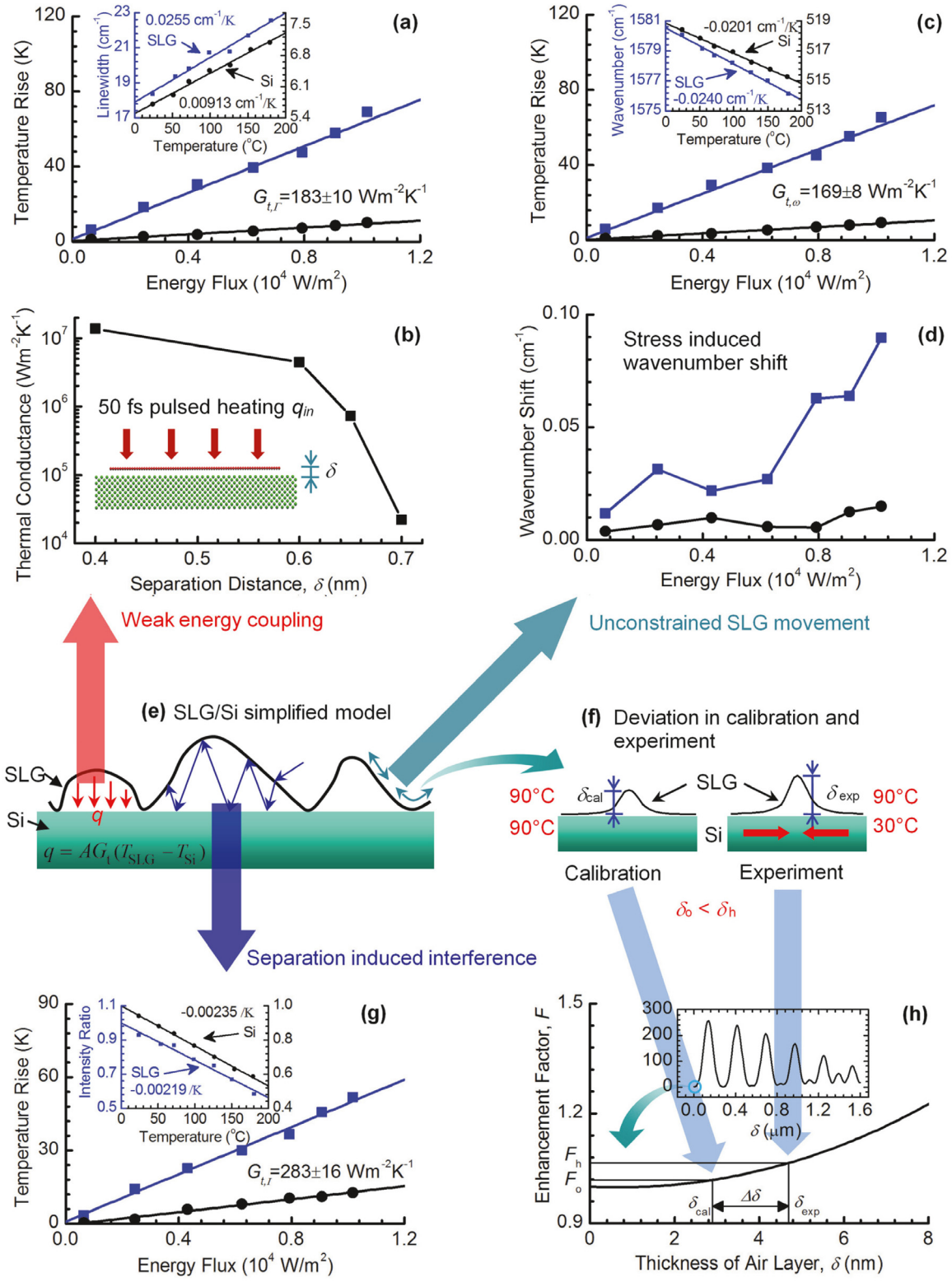


**Fig. 6.** Interface optical interference effect study in unconstrained SLG/Si interface. (a) The temperature coefficients of SLG and Si Raman peaks and the thermal conductance at the SLG/Si interface determination based on linewidth. (b) Numerical study shows the interfacial thermal conductance/energy coupling weakening effect by separation widening between SLG and Si. (c) The temperature coefficients of SLG and Si Raman peaks and the thermal conductance at the SLG/Si interface determination based on Raman shift. (d) Stress induced Raman shift for SLG and Si is very little as the shift is negligible. (e) A simplified schematic of the weak energy coupling at the SLG/Si interface, including unconstrained SLG movement and separation induced interference at the interface. (f) Variation of the spacing layer in the experiment and calibration due to the thermal expansion mismatch between SLG and Si. (g) Interface optical interference effect induced additional Raman intensity increase for SLG and Si against heating laser heat flux. (h) Increment of the Raman intensity enhancement factor (F) of SLG with the thickness of separation layer ($\delta$). (Reprinted with permission from [11]. Copyright (2014) American Chemical Society)

other. However, in some areas, there existed separations between the two materials, causing multi-reflectance of incident laser and scattering and, consequently, Raman intensity enhancement. Furthermore, the air spacing impeded the thermal energy coupling across the interface due to its low thermal conductivity. An obvious temperature difference was observed between the two surfaces at the interface. Due to this temperature difference, the graphene layer and the substrate showed different thermal expansion behaviors from those at the same temperature in thermal calibration. Additional distance was increased in the graphene/Si substrate interface as shown in Fig. 6(h). This interface optical interference effect would largely increase the measured Raman intensity and introduce errors in Raman-intensity based temperature measurement and interface thermal resistance characterization.

The choice of Raman temperature measurement method is based primarily on the quality of the sample and experimental conditions. Raman intensity-based temperature measurement requires the sample to remain extremely stationary during experiment. Movement caused by backlash in any direction of the sample stage would not be preferred. The Raman wavenumber-based temperature measurement requires accurate determination of the Raman peak position. Gaussian and Lorentz shape fitting could help to better acquire the shift of Raman peaks. Also, sound Raman signals and high resolution of Raman spectroscopy are preferred in order to obtain an accurate wave number change. The Raman linewidth-based measurement could be used in the higher temperature ranges and under the scenario of existing mechanical stress as it is least sensitive to stress [6,63]. However, when sample quality is pretty good (high crystallinity and little lattice defects) and the Raman excitation laser's intensity is high enough, the measured Raman signal (Stokes peak) will be strong, and each of the above three methods could work well. If the sample has a significant thermal expansion, it would affect the focusing level of the laser at the sample's surface, so only the Raman wavenumber- or linewidth- based method could be selected. When using the wavenumber-based method for temperature measurement, if the type of sample (preparation method, lattice structure, etc.) or the type of laser (wavelength, energy, etc.) changes, the temperature coefficient of the sample needs to be recalibrated.

### 2.5. Calibration of Raman-response to temperature: accuracies and uncertainties

#### 2.5.1. Strongly structure-dependent Raman properties and temperature coefficients

In Raman-based temperature measurement and thermal transport characterization, the temperature coefficient is a key parameter to calculate the temperature rise in materials. It is almost a constant for each property (shift, linewidth, and intensity) in a certain temperature range: from room temperature to 1000 K for silicon as an example. Thus, the temperature in the Raman-based method can be easily determined using:

$$T = T_0 + \left(\frac{\partial X}{\partial T}\right)^{-1}(X - X_0). \tag{4}$$

$X$ represents one property. However, the temperature coefficient strongly depends on the Raman excitation laser and may vary to different Raman excitation sources. Take graphene as an example, the temperature coefficient of Raman shift of graphene was measured to be in the range from -0.015 to -0.076 $cm^{-1}/°C$ for the G-band using different lasers [66-68]. Yue's work showed a temperature coefficient of -0.016 $cm^{-1}/°C$ from room temperature to 250 °C by using a 532 nm laser [8]. Balandin measured the thermal conductivity of single-layered graphene based on the temperature coefficient of -0.015 $cm^{-1}/°C$ [69]. In Calizo's work, the temperature coefficient of graphene was determined to be -0.016 $cm^{-1}/°C$ for a single layer and -0.015 $cm^{-1}/°C$ for bilayer using a 488 nm laser [70]. Zhao *et al.* studied the graphene on $SiO_2$ substrate and the temperature coefficient was calibrated to be -0.031 ± 0.005 $cm^{-1}/°C$ from 20 to 100°C [71]. Nguyen *et al.* found the temperature coefficient is round -0.03 $cm^{-1}/°C$ after several annealing cycles [72]. Wang *et al.* studied the temperature coefficient of graphene deposited on copper coil in the lower temperature range from 150 K-390 K, and found the coefficient was less than -0.089 $cm^{-1}/°C$ [73].

It has been proved that the temperature coefficient varies with the number of graphene layers. Since the temperature dependence of Raman shift is determined by the inharmonic interaction of the phonons, the coefficients are different for materials with different structures or if different probing lasers are used [74]. The Raman shift against temperature can be regarded linear over a small temperature range, but different temperature ranges will vary the temperature coefficients in the calibration. Therefore, calibration is necessary for each sample measured in a defined Raman system.

A widely adopted procedure for Raman properties/temperature calibration can be concluded as followings [8,10,65,75-77]. A sample is placed on a heating stage, so the heating stage could heat the sample up uniformly. The whole sample-heating setup is further fixed on 3D stage and could be moved in three directions. The sample is heated to an expected temperature, and a long setting time guarantees that the sample could reach a thermally steady state at the same temperature as the heating stage. Raman spectroscopy records the spectrum corresponding to this temperature. Then the heating stage will be set to another temperature to obtain another Raman spectrum. After repeating the same process several times, a series of Raman spectra against temperature will be obtained. Further analysis will uncover the relations between wavenumber, linewidth, and intensity of a Raman peak against temperature.

#### 2.5.2. Undesired physics deviation in calibration and thermal characterization

In the aforementioned calibration, the focusing issue should be carefully addressed. As mentioned in Section 2.4, the heating power will also raise the temperature of the heating stage itself and the sample stage. Both stages will thermally expand largely in all directions. Thus, the overall thermal expansion in the $z$ direction will move the sample away from the focal level. Repeating refocusing the sample to the focal level is exactly what has been done in previous temperature coefficient calibrations. Furthermore, heating up in the sample/stage will give some non-negligible effects on the objective lens and the surrounding air. This issue has not been sufficiently addressed in the past. This is part of the reasons that even for the same material, the temperature coefficient of Raman shift varies from literature to literature. Take silicon wafer as an example, the temperature coefficient for the Raman wavenumber of c-Si ranged from -0.019 to -0.0355 $cm^{-1}/°C$ under different $MoS_2$ samples of different layers [17]. Tang calibrated the temperature coefficient to be 0.0201 $cm^{-1}/°C$ for the wavenumber of the same type of silicon wafers as above under unconstrained graphene layer [11]. This coefficient was -0.0264±0.0012 $cm^{-1}/$ °C for c-Si substrate in Yuan's work [18]. Thus, for c-Si wafer, the calibrated temperature coefficient is around -0.0252 $cm^{-1}/°C$ with a possible error of ±0.0062 $cm^{-1}/°C$.

For supported 2D materials, in the calibration the stress is introduced by the different thermal expansion behaviors and different temperature states in two materials from that of thermal transport characterization and would raise more errors in the calibrated temperature coefficients. In calibration, the entire sample (top film and beneath substrate) is heated up uniformly to the same temperature. No temperature gradient exists in both. How-

ever, due to the different thermal expansion coefficients of the 2D material and substrate, a stress will be built up in the 2D material due to thermal expansion mismatch. In contrast, in Raman-based thermal probing, the exciting laser is well focused to a small spot on the sample's surface using objective lenses. The spot diameter is around several microns and usually much smaller than the 2D material sample's size. The sample is heated up very locally, and a very large temperature gradient arises, inevitably resulting stress in the 2D material. The temperature of the substrate/supporting material, however, does not rise much because of its high thermal conductivity for Si or low absorption of the heating laser for glass. Also, the thermal interface resistance between the 2D material and the substrate will impede part of thermal energy transfer across the interface. Compared with the case in the calibration, the temperature of the substrate is much lower than the sample. Since the 2D material and substrate have different temperature rises, the final thermal expansion mismatch-induced stress in the 2D material will be different from that in calibration. Therefore, the calibration results are not able to give sound temperature evaluation in thermal characterization.

Directly using the calibrated Raman shift temperature coefficient will lead to finite, yet sometimes nonnegligible temperature rise calculation errors. This was rarely addressed in most previous work. Tang *et al.* made great effort to distinguish the effect of this stress on Raman-based thermal measurement. Utilizing the different response to stress of Raman linewidth and shift, the conjugation of temperature field and stress field could be distinguished [9,63]. Since the stress has the negligible effect on Raman linewidth, the temperature measurement based on Raman linewidth broadening could represent the real temperature of the sample. The temperature from Raman shift, however, included the stress-induced shift and would be higher or lower than the real temperature which should be independent of stress. Consequently, the temperature difference resulted from the two methods was directly related to stress and could be used to determine the stress in quantity.

The contraction in the substrate will also produce or enlarge the gap between the 2D material and the substrate [10,65] due to the thermal expansion mismatch between the 2D material and substrate. The Raman intensity could further show us more information about how large the gap is between the sample and the substrate. Temperature rise, stress, and interface gap could all significantly affect the accuracy for temperature measurement using the intensity-based method. After the determination of temperature and stress using the above method, it is able to find out the optical interference-induced intensity change. The Raman intensity enhancement is due to factors: enhancement of the laser absorption and the enhancement of the Raman intensity emitting out. A normalized enhancement factor was introduced in previous work [10,64,65,78] for the laser absorption:

$$\mathrm{F}_{ab} = t_1 \frac{(1 + r_2 r_3 e^{-2i\beta_2}) e^{-i\beta_x} + (r_2 + r_3 e^{-2i\beta_2}) e^{-i(2\beta_1 - \beta_x)}}{1 + r_2 r_3 e^{-2i\beta_2} + (r_2 + r_3 e^{-2i\beta_2}) r_1 e^{-2i\beta_1}}, \tag{5}$$

where $t_1 = 2n_0/(n_0 + \tilde{n}_1)$, $r_1 = (n_0 - \tilde{n}_1)/(n_0 + \tilde{n}_1)$, $r_2 = (n_1 - \tilde{n}_2)/(n_1 + \tilde{n}_2)$, and $r_3 = (\tilde{n}_2 - \tilde{n}_3)/(\tilde{n}_2 + \tilde{n}_3)$ are the Fresnel transmittance and reflection coefficients for the interfaces involving air (0), nano-materials (1), air (2) and substrate (3). $n_m$ is the refractive index for the involved materials, $m = 0, 1, 2, 3$. $\beta_x = 2\pi x \tilde{n}_1/\lambda$, $\beta_1 = 2\pi d_1 \tilde{n}_1/\lambda$, and $\beta_2 = 2\pi d_2 \tilde{n}_2/\lambda$, where $x$ is the depth of the point where interaction occurs, $\lambda$ is the wavelength of the incident laser, and $d_1$ and $d_2$ are the thickness of nano-materials and the gap in-between.

The net scattering enhancement factor ($F_{sc}$) (for the enhancement of the Raman signal emitting out) is described as

$$F_{sc} = t_1' \frac{(1 + r_2 r_3 e^{-2i\beta_2}) e^{-i\beta_x} + (r_2 + r_3 e^{-2i\beta_2}) e^{-i(2\beta_1 - \beta_x)}}{1 + r_2 r_3 e^{-2i\beta_2} + (r_2 + r_3 e^{-2i\beta_2}) r_1 e^{-2i\beta_1}}, \tag{6}$$

where $t_1' = 2\tilde{n}_1/(n_0 + \tilde{n}_1)$ and in the scatterings, the wavelength in $\beta$'s become the wavelength of Raman scatterings. Thus, the total enhancement factor of Raman signal ($F$) is given by

$$F = N \int_0^{d_1} |F_{ab} F_{sc}|^2 dx, \tag{7}$$

where $N$ is a normalized factor, which is a reciprocal number of the total enhancement factor for the layered structure without a gap between them, obtained by setting the thickness of the air layer in-between to be 0. The thickness of gap could be easily obtained by comparing the real intensity enhancement with a theoretical one based on Eqns. (5-7). Fig. 6(h) shows how the enhancement factor varies against the separation distance of a single layer graphene/Si interface. In conclusion, the calibration could present a quite different scenario from that in optical based heating and Raman probing. To mitigate this issue, the temperature rise in both calibration and thermal characterization should be kept to the lowest level as long as the signal-to-noise ratio is good. Also, it is feasible to evaluate the temperature rise using both Raman shift and linewidth and evaluate the effect of stress.

## 3. Steady-state Raman-based Characterization: Heating Level Evaluation

In the thermal characterization of nanoscale thermal transport based on steady-state Raman thermometry, two critical factors are needed: temperature rise of the interested sample and heating level. The thermophysical properties, thermal conductivity in particular, can be directly obtained by the two factors, which makes accurate temperature measurement and heating level evaluation are important. The influence factors and points for attention of temperature measurement have been detailed discussed in Section 2. Thus, this section will introduce the problems of heating level evaluation caused by direct laser absorption measurement, and some other feasible evaluation approaches in steady-state measurement.

### 3.1. Problems in direct measurement to determine laser absorption

In Raman-based thermal transport characterization, the heating level in the material is a critical parameter and will introduce large errors in the final measurement result when it is miscalculated. For nanomaterials, like 2D atomic layer materials, the light absorption is very weak. One way to determine the light absorption is to directly measure the transmittance and reflectance by placing a detector under/above the 2D material layer, and subtract them from the total incident light. This usually introduces significant errors in the measured results as the power meters may not be so sensitive to such little absorption in the atomic layer sample. Great efforts have been applied to measure the optical properties of 2D material layer. Take graphene as an example, Mak *et al.* experimentally studied the optical conductivity of graphene [79]. They have found that the optical absorption of single layer graphene is round 2.3%. Nair *et al.* investigated the effect of the number of layers of graphene on its optical absorption, and the absorption was found to increase almost linearly with the number of layers [80]. In Balandin's work, the power absorbed in graphene was determined by $P = I_0 A(1\text{-}\exp(-\alpha_G \delta_G))$, where $A$ is the illuminated area, $I_0$ is the laser intensity on the surface, $\alpha_G$ is the absorption coefficient, $\delta_G$ is the monolayer thickness [81].

Furthermore, the optical absorption depends on the wavelength of the incident laser, and can also be affected by stress/strain, defects, contaminations and near-field or multiple reflection effects [21,22,82]. This could be one of the main causes for large deviations in the measurement of thermal conductivity and interface

thermal conductance. An alternative way is to use electrical heating instead of optical heating since the Joule heating could be very well defined [8,83]. A new route has been developed to combine the Raman-based temperature measurement and electrical heating method for accurate thermal characterization of nanomaterial.

### 3.2. Accurate heating control and evaluation by combined Joule heating and laser heating

Yue, *et al.* did the first work on Joule-heating experiment for the thermal contact resistance measurements with combination of the electrical heating and Raman-based temperature probing. The principle of the measurement is shown in Fig. 7. A few-layered graphene was placed on a SiC substrate and fixed by two electrodes on its two ends. A current $I$ was fed through the graphene layer as it is electrically conductive with a certain electrical resistance $R$. Thus, a defined thermal energy input could be directly determined according to Joule heating. Since graphene has an extremely high thermal conductivity, the temperature rise was assumed to be uniform in the graphene layer, and the generated heat mainly dissipated across the interface to the substrate. A Raman excitation laser of low power was focused on the graphene layer to probe the temperature of both graphene layer and SiC substrate, $T_{\text{graphene}}$ and $T_{\text{SiC}}$, simultaneously. The temperature rise caused by the laser is ruled out by studying the temperature change of sample against the Joule heating power. Thus, the interfacial thermal resistance could be further determined with above information using $R_{\text{tc}} = (T_{\text{graphene}} - T_{\text{SiC}})\bullet(I^2R)$. Both the thermal and electrical contact resistances at the electrodes were carefully treated by adding little silver paste at the contact points. Using the combined method, the $R_{\text{tc}}$ between graphene and SiC was measured to be $5.30\times10^{-5}$ K•m$^2$/W, well agreeing with $1.01\times10^{-4}$ K•m$^2$/W of the same sample in the independent laser heating measurement.

Wang *et al.* developed an electrical heating assisted Raman method to capture the thermal conductivity and optical absorption coefficient of the same micro/nano wire simultaneously [84]. In this method, an electrical current was used to heat an individual suspended CNT, while its temperature rise was measured by monitoring its Raman shift. The temperature rise by the incident laser was considered. A weak laser beam was focused on the CNT to collect Raman signal, and it would cause unavoidable temperature rise of several kelvins. In order to eliminate the influence caused by laser heating, the laser power was kept constant and the temperature difference before and after switching on the electrical current was measured in the experiment.

Fig. 8 shows the G-band wavenumber shift of suspended CNT under the electrical heating and laser heating conditions. In data analysis, the first step was to calculate the thermal conductivity of CNT based on the measured temperature rise and corresponding Joule heating power, giving a value of 2630 W/(m•K). After switching off the electrical power, laser was the only heating source for CNT. Taking the thermal conductivity of CNT as a known parameter, the optical absorption coefficient of CNT remained is the only unknown parameter. The laser power distribution along CNT can be well described by a Gaussian function. Substituting the measured thermal conductivity and temperature rise due to laser heating into the heat conduction equation, the optical absorption coefficient of single CNT was calculated to be 0.194%.

### 3.3. Simultaneous optical absorption coefficient determination

Another way to evaluating the optical absorption coefficient of CNT is the T-type thermal probe method, proposed by Li *et al.* [85]. A suspended CNT was attached to a free-standing Pt nanofilm at one end, forming a T-type probe. Then a laser beam was focused on the suspended CNT as a heat source. The average temperature rise of CNT was measured through the electrical resistance change of Pt film. Ignoring the convective heat transfer and thermal radiation, the absorbed laser power in CNT can be calculated by a simple heat conduction model with the measured temperature rise as known parameter. Then the optical absorption coefficient was determined as the ratio between the absorbed and input laser power. For a multiwall CNT with 100 nm diameter, the optical absorption coefficient is measured as 13.2%. It is found that the optical absorption coefficient of CNT is roughly proportional to its diameter.

With the knowledge of optical absorption of individual SWCNT, Liu *et al.* measured the length dependent thermal conductivity of pristine SWCNT [86]. An ultra-long SWCNT was grown on a silicon substrate with different trenches by using a CVD method. An experimental schematic diagram is shown in Fig. 9.

As shown in Fig. 9, there are two methods to change the length of heat conduction in SWCNT. The first method is to suspend a SWCNT over a series of trenches with different linewidth and the probing laser is focused on each segment with different lengths. The second method is to suspend a long SWCNT over a wide trench and the focused laser is moving along the sample. In the latter one, heat is conducted from the focusing center to the heat sinks through the left and right segments, which are connected in parallel. By solving a parallel thermal resistance model, the length dependent thermal conductivity of SWCNT can be obtained.

Fig. 10 shows the length dependent thermal conductivity of SWCNT, where different thermal contact resistances are chosen for calculation. It is observed that the thermal conductivity of SWCNT increases with increased length and saturates around 10 $\mu$m. The two methods of changing trench linewidth and changing laser spot position give the similar trend of thermal conductivity, and the different thermal contact resistances do not change the trend much. For short CNTs, the mean free path (MFP) of phonons increases with increased sample length, where the boundary scattering at two ends play a significant role. For long CNTs, the boundary scattering becomes less important and the Umklapp scattering is dominant, resulting in a constant thermal conductivity.

Based on the precisely measured thermal conductivity and optical absorption coefficient of single CNT, Wang *et al.* managed to measure the heat transfer coefficient between an individual SWCNT and surrounding air molecules [85]. The measurement principle was almost the same as the one described above, except the additional heat transfer term in the governing equation to address the interactions between SWCNT and air molecules. In data analysis, the thermal conductivity and optical absorption coefficient of SWCNT were measured beforehand, leaving the heat transfer coefficient as the only unknown parameter. Substituting the measured temperature rise of SWCNT into the heat conduction equation, the heat transfer coefficient $h$ could be decided.

If a suspended SWCNT is heated by a large electrical current, the heat flux along the nanotube may exceed $10^{11}$ W/m$^2$ due to its extremely small cross-sectional area and an extremely high temperature gradient will be built. Liu *et al.* obtained the temperature distribution along a suspended SWCNT under large electrical current heating conditions [86]. The local temperature of SWCNT was measured through its G-band Raman peak shift and the spatial resolution was about 5 $\mu$m, mainly limited by the size of focused laser spot. The temperature dependent thermal conductivity of SWCNT was measured simultaneously in the experiment. The result indicates that the Fourier's law still holds true at the nanoscale under extremely high heat flux ($10^{11}$ W/m$^2$) conditions. On the other hand, knowing the spatial temperature distribution, one can easily calculate the thermal contact resistance between the nanotube/wire and substrate [87].

Through combining the electrical heating and laser heating, Liu *et al.* measured the thermal conductivity and laser absorptivity of graphitized carbon fiber sample and the thermal contact resistance

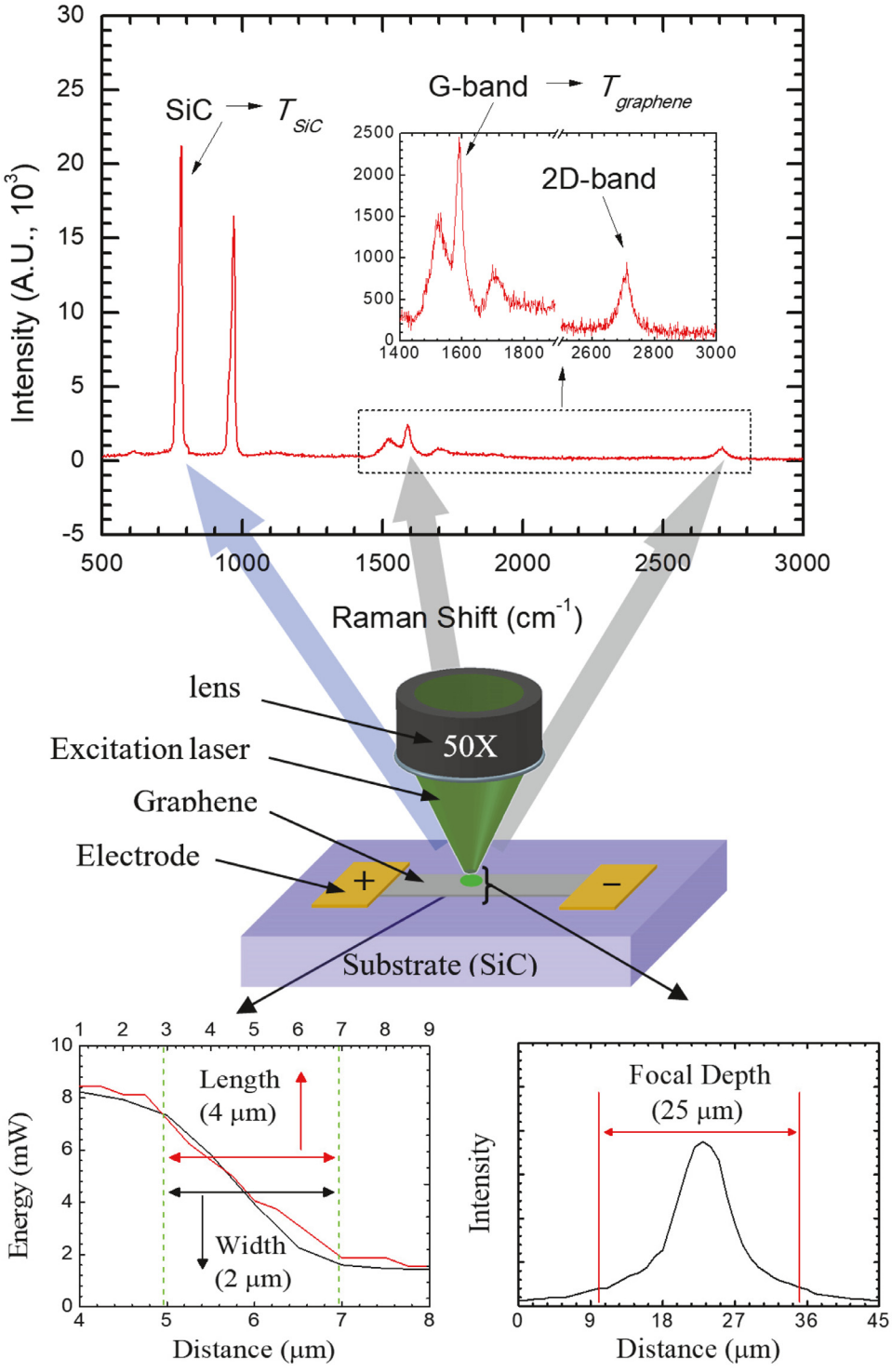


**Fig. 7.** Principle of the Joule-heating experiment used for the thermal contact resistance measurements. (a) The sample Raman spectrum of epitaxial graphene on 4H-SiC (0001). (b) The scheme of experimental setup for the thermal contact-resistance measurement. (c) The spot size of the laser is determined to be 4 $\mu$ m × 2 $\mu$ m. (d) Focal depth of lens is determined as 25 $\mu$m from the evolution of Raman intensity when the lens approaches the sample. (Reprinted from Ref. [8]. Reproduced with permission of Wiley. All rights reserved)

between the sample and heat sink [88]. As shown in Fig. 11, the suspended sample is simultaneously heated by Joule self-heating and a focused laser spot. In a vacuum chamber, both the convective and radiative heat transfer was neglected compared with conductive heat transfer. To cancel the unknown laser absorptivity, the electric power is changed from $I_1U_1$ to $I_2U_2$, and then the laser absorptivity can be eliminated by comparing two independent energy conservation equations with two measured temperature rises $\theta_{L/2,1}$ and $\theta_{L/2,2}$. To separate the thermal conductivity and thermal contact resistance, the focused laser irradiates at two different positions with two different laser power $P_1$ and $P_2$, and the measured temperature rise is $\theta_1$ and $\theta_2$.

With the determination of thermal conductivity $k$ and the thermal contact resistance between the sample and the heat sink $R_c$,

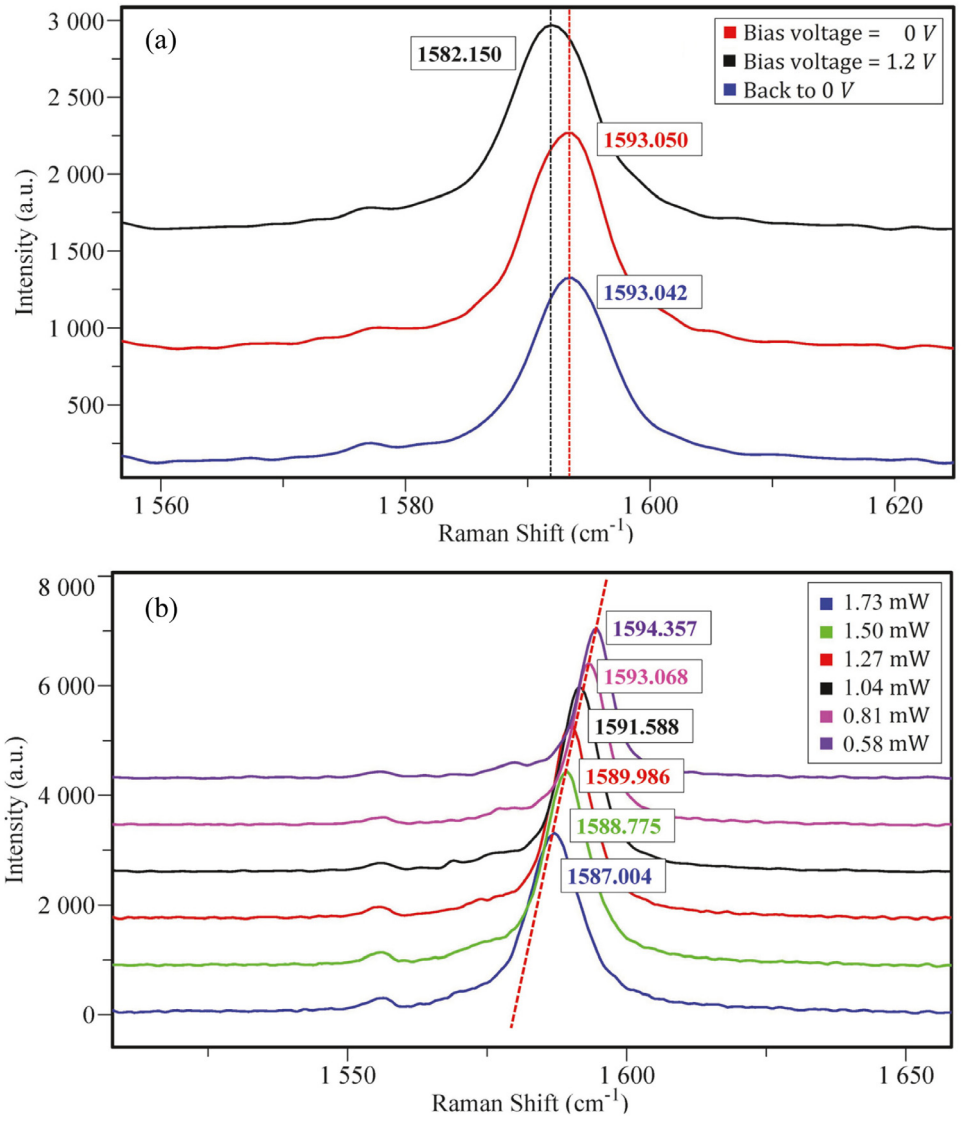


**Fig. 8.** Raman shift of suspended CNT caused by electrical heating (a) or laser heating (b). The Raman shift of G-band peak is given in the figure for comparison. (Reprinted from Ref. [84]. Reproduced with permission of IOP Publishing. All rights reserved)

by measuring two different powers $P'$ and $P''$, the local temperature change at the irradiation point is defined as $\Delta\theta$, then the laser absorptivity can be determined using Eq. (8).

$$\alpha = \left[\frac{\Delta\theta}{L_1/(kA)+R_c} + \frac{\Delta\theta}{L_2/(kA)+R_c}\right] / \left(P' - P''\right), \tag{8}$$

where $L_1$ and $L_2$ are the distances from the laser spot to the two heat sinks.

Though the Joule heating method can offer well-defined heating energy input, the electrodes are hard to prepare. The common methods to prepare micro/nano-electrodes include photolithography, nanoimprint [89], and nanotransfer printing [90]. In these processes, complex steps are needed and a long preparation time is necessary, which largely increases the difficulty in sample preparation and field/measurement application.

### 3.4. Optical heating evaluation based on optic calculation

Another way to evaluating the laser absorption in 2D materials is to use the reported optical properties and directly calculate how much laser power is absorbed [91]. Three issues in this method usually raise a lot of deviation in measurement results. First, the reported optical refractive index in literature could be different from the one of the material used in thermal characterization due to sample synthesis, defects, and impurity level [79,80]. Even for the same material, the reported optical index could vary significantly because of the optical measurement methods and errors. For example, the refractive index of $MoS_2$ is ~3.05 determined by spectroscopic ellipsometry [92] and ~5.2 (1.7 times larger) by a spatially resolved spectrum system [93].

Second, the very tiny, yet unknown spacing between the 2D material and the substrate will give very strong optical interference, and significantly affect the absorbance. The newly appeared spacing will introduce one more interface, and more reflections will happen than that in the case without spacing. Variation in Raman scattering signal enhancement has been observed and proved theoretically [64] and experimentally [11]. In both works, an enhancement factor has been defined to describe the total increase in absorption of incident beams and scattering beams of the interested layer. The theoretical study shows that the enhancement factor of graphene on a silicon substrate with a layer of $SiO_2$ in between has tripled when the thickness $SiO_2$ layer increases from 0

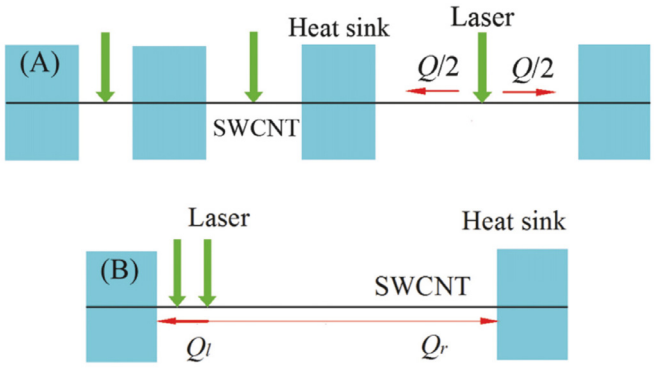


**Fig. 9.** Schematic diagram for measuring SWCNT with different lengths. (a) The same SWCNT is suspended over trenches of different linewidths and the probing laser is focused on each segment. (b) A long SWCNT is suspended over a wide trench and the focused laser is moving along the sample. (Reprinted from Ref. [86]. Reproduced with permission of The Royal Society of Chemistry. All rights reserved)

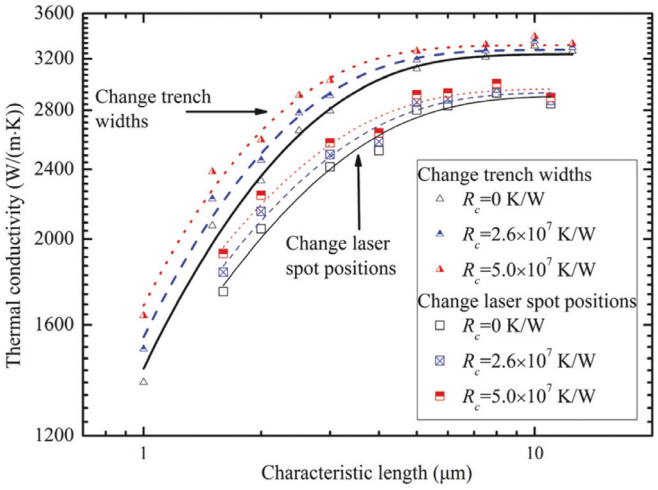


**Fig. 10.** Length dependent thermal conductivity of SWCNT. Different symbols represent the result calculated by using different thermal contact resistances. (Reprinted from Ref. [86]. Reproduced with permission of The Royal Society of Chemistry. All rights reserved)

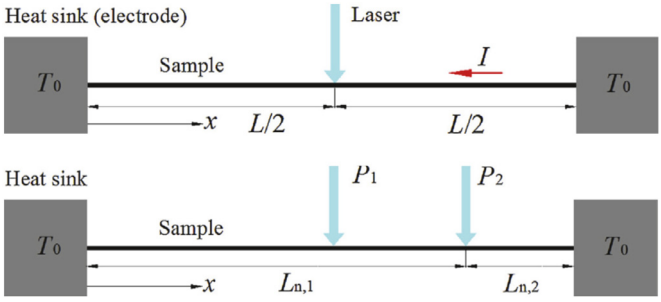


**Fig. 11.** Schematic of the measurement principle for separating the thermal conductivity and thermal contact resistance. (Reprinted from Ref. [88]. Reproduced with permission of Elsevier. All rights reserved)

to 100 nm [64]. In Tang's work, a separation increment of 1.8 nm for the graphene on a silicon substrate with an air gap in between gave a 4.5% increase in the measured enhancement factor [11].

Third, in the optical absorption calculation [81], the light is usually assumed normal to the tested material. In experiment, the light comes with a certain numeral aperture. That is: parallel incident light is focused and become a conical beam when it arrives at the surface. The light passes through the outer place will have a larger incident angle, while the light comes in the center of the lens has a smaller one, so that all the lights can pass through the same point of incidence. When the light arrives at the sample's surface, only the light beams in the center will be perpendicular to the surface. The angle of incidence of other rays will vary and thus the amount of light energy reflected and transmitted may vary according to the incident angle.

Tang investigated the absorption of an incident laser for samples [11]. A heating laser came in with an incident angle of 60°. The laser was first passed through a glass substrate and maintained 92.4% energy when reaching the graphene next to the glass substrate. The laser absorption coefficient was determined using the refractive indices of graphene, glass, and air, and the propagation path was calculated based on the incident angle. A total absorption of 2.63% laser energy by the single layer graphene was found after four reflection processes of light. Given the Raman incident light composed of laser rays with different incident angles, all these will combine together to give enormous, yet not well-known uncertainty in the laser beam absorption. This uncertainty directly propagates to the final results and gives very large uncertainties in the measured thermal conductivity and interface thermal conductance.

In summary, the uncertainty comes with the not well-defined heating level and raises a large deviation in the final measured thermal properties. One way to resolving this issue is to conduct the measurement in time or frequency domains without needing the knowledge of the light absorption.

## 4. Temporal Raman-based Characterization: Frequency and Time Domains

For Raman measurement at steady states, careful evaluation and calibration of the optical absorptivity is essential for performing precise thermal characterization. However, this process can be very challenging and time-consuming, especially for micro/nano materials. The characterization of transient parameters, like thermal diffusivity, is also missing in the steady-state methods. More importantly, the steady state Raman method is based on the assumption that all phonon modes are in thermal equilibrium and have the same temperature in the Raman excitation laser spot. The recent work of Vallabhaneni *et al.* [94] revealed that strong nonequilibrium exists among different phonon branches in single-layered graphene under laser irradiation. The incident photons excite electrons and generate hot electrons fast due to fast electron-electron scattering. Then the electrons relax and release energy to in-plane optical phonons (TO and LO). These phonons function as an energy receiver and transfer energy to in-plane acoustic phonons and out-of-plane phonons through phonon-phonon scattering. This phonon-phonon scattering is proved to be at strong nonequilibrium, so the acoustic phonons have a lower temperature than the optical phonons, but they are responsible for transferring heat to heat sinks and contribute to the 2D materials' thermal conductivity. Thus, the measured temperature from Raman spectrum is the temperature of optical phonons, and could not reflect the real temperature (acoustic phonons) in 2D material and so as to the measured thermal properties.

To overcome the challenges induced by heating level evaluation, calibration, and inevitable deviation in temperature, one alternative and very promising way for thermal characterization using Raman spectroscopy is to use a temporal characterization concept. It characterizes 2D material's transient thermal response and determines its thermal diffusivity and normalized interface conductance $G/\rho c$ ($\rho$ and $c$: density and specific heat of the material of interest; $G$: interface thermal conductance). Since the 2D material's density and specific heat have negligible difference from those of the bulk counterpart, the sample's thermal conductivity and interface thermal conductance can be determined readily with high confidence.

In the past, the transient way has been proved to work overwhelmingly well to characterize the thermal diffusivity of materials. A material's density and specific heat can be measured very precisely using various available techniques. The transient measurement techniques include the hot-wire technique for liquid measurement [95], photothermal method for coating measurement [96,97], pump-probe method for coating measurement [98-101], and laser flash method for disk-like material measurement. All these techniques have become the golden standards in thermal characterization. To overcome the challenges in the steady-state Raman measurement and utilize the advantages of transient methods, temporal Raman-based characterization methods were recently developed in Wang's [14,15,18,22] and Zhang's groups [12,13,16,23-25,87,102].

### 4.1. Time-domain differential Raman (TD-Raman)

Four techniques have been established in Wang's lab for transient Raman thermal characterization: time-domain differential Raman (TD-Raman) [14], frequency-resolved Raman (FR-Raman) [15], and energy transport-state resolved Raman (ET-Raman) [18,21], and frequency-domain ET-Raman (FET-Raman) [22]. TD-Raman was the first one designed for realizing the transient thermal probing using Raman technique. As shown in Fig. 12, the TD-Raman employed a carefully designed pulsed laser for both heating and Raman excitation. The pulsed laser consisted of a varied pulse-on period and a fixed pulse-off period. During the laser pulse-on period, the tested sample was heated up and the length of the pulse-on period varies from a very short one to a sufficiently long one. In those short periods, the sample cannot reach the thermally steady state when the laser is on. As the pulse-on period becomes longer, the sample could be closer to the thermally steady state until the sample can reach the steady state. The pulse-off period is long enough for the sample to completely cool down to the room temperature before the next pulse comes in.

Evaluation of the TD-Raman method was conducted on a tipless Si cantilever. The cantilever has an approximately 1-dimensional shape and the Raman laser was focused on its tip end. The laser heated the tip and the generated thermal energy would dissipate along the cantilever to the chip (heat sink). Note in TD-Raman, the temperature reflected by the Raman spectrum is an average over the whole heating time and the space covered by the laser spot $\bar{\theta} = \int_0^{t_e}\int_{x_1}^{x_2}\theta(x,t)dxdt/(x_2-x_1)t_e$. It can be expressed as:

$$\bar{\theta} = \frac{2\dot{g}L^3}{(x_2-x_1)kt_e}\sum_{m=1}^{\infty}\frac{1}{m^4\pi^4}\left(1+\frac{L^2}{m^2\pi^2\alpha}e^{-m^2\pi^2\alpha t_e/L^2}\right) \times\left(\cos\frac{m\pi}{L}x_1-\cos\frac{m\pi}{L}x_2\right)^2, \quad (9)$$

where $x_1$ and $x_2$ are the coordinates of the heated region in this 1-D model. $\alpha$ is the thermal diffusivity, $L$ is the length of the sample, $t_e$ is the heating duration, $k$ is the thermal conductivity, and $\dot{g}$ is the heat induced by the incident laser on the sample. In data processing, this should be taken into consideration in order to determine the thermophysical properties with great accuracy. Since the pulse interval is long enough, the sample does not have heat accumulation. Therefore, the thermal response of the sample can be strictly determined by the temporal square-wave heating source.

Based on the length of the cantilever and the reference value of silicon's thermal diffusivity, a laser-on time span was then carefully designed from 20 $\mu$s to 2 ms to cover the time length in which the tip would reach steady state in this heating condition. By fitting the variation of Si Raman peak against time, using 1-D transient heat transfer physical model, the thermal diffusivity was determined to be $9.17\times10^{-5}$, $8.14\times10^{-5}$, and $9.51\times10^{-5}$ m$^2$/s from the normalized Raman peak intensity, shift, and peak area against the heating time. They were all within 10% errors of the reference value of thermal diffusivity for silicon.

### 4.2. Frequency-resolved Raman (FR-Raman)

The TD-Raman technique realizes the first Raman characterization of the transient heat transfer process in low-dimensional materials. However, it still has one obvious technical drawback: when the heating time is extremely short, ~20 $\mu$s in the above-mentioned evaluating experiment, the integration time in the Raman spectroscopy would become as long as half an hour to get a sound Raman spectrum. This long integration will introduce more environmental interference to the experiment, and lower the measurement accuracy. One way to solving this issue is to use the frequency-resolved Raman (FR-Raman) method [15], which is an advanced technique developed in Wang's lab. The FR-Raman technique redesigns the duty of the pulsed laser based on TD-Raman technique, and extends its measuring capability to probe a very fast transient thermal transport at the scale of microsecond to nanosecond. Meanwhile, it could provide a sound spectrum with a sufficient signal-to-noise ratio for data processing.

FR-Raman still uses the pulsed laser as heating and exciting sources as shown in Fig. 13, but the pulse duty is kept to be 50%. That means the laser is on in half time of a period and is off in the other half. In this way, Raman signal is always collected in half of the integration time, and will become much stronger compared with TD-Raman. However, since the cooling time between pulses is not enough for the sample to cool down completely, FR-Raman will have less theoretical sensitivity in thermal characterization compared with TD-Raman.

In FR-Raman, since the pulse interval is not sufficiently long to allow the sample to cool down, heat accumulation occurs, and a quasi-steady state was then defined when the modulation frequency is very large. The temperature rise in quasi-steady state was the half of the temperature rise at thermally steady state. That means many pulses will need to be calculated in numerical modeling to obtain quasi-steady state response of the system to periodical laser heating. This could be very time consuming numerically since there are rare analytical solutions for the physical problems under study. Such data processing obstacle has been overcome by constructing the periodical heating source in the heat transfer governing equation to consist of many step function heating sources. Analogous to TD Raman, an evaluation experiment was carried out using the same type of the silicon cantilever. For laser heating of a micro-scale Si cantilever, the temperature response probed by the Raman can be expressed as

$$\bar{\theta}(t)_{pulse} = C_0\sum_{m=1}^{\infty}C_m\left[1-e^{-m^2\pi^2\alpha t/4l^2}/\left(1+e^{-m^2\pi^2\alpha/(8f_0l^2)}\right)\right], \quad (10)$$

where $C_m = \{[1-(-1)^m]\cos[m\pi x_1/(2l)]\}^2/(m^4\pi^4)$ and $C_0 = 8\dot{g}l^3/[(l-x_1)k]$. Besides, $x_1$ and $x_2$ define the heated region on the micro-scale Si cantilever. $\alpha$ and $k$ is the thermal diffusivity and thermal conductivity of Si. $l$ is the effective length of the cantilever after fully considering the geometry of the cantilever's end. $f_0$ is the modulation frequency, and $\dot{g}$ is the heat induced by the incident laser on the sample. The thermal diffusivity of the Si cantilever was determined at $9.57\times10^{-5}$ m$^2$/s, $11.00\times10^{-5}$ m$^2$/s, and $9.02\times10^{-5}$ m$^2$/s through intensity, shift, and total Raman emission, respectively.

Despite the less sensitivity of FR-Raman method, its most important advantage is that the collection of Raman signals becomes more efficient than TD-Raman. Take the 20 $\mu$s-laser-on-each-period case in the Si cantilever evaluating measurement as an example: In TD-Raman it took 100 s to get a sound Raman spectrum, while only 2 s in FR-Raman. Also, in FR-Raman, the inte-

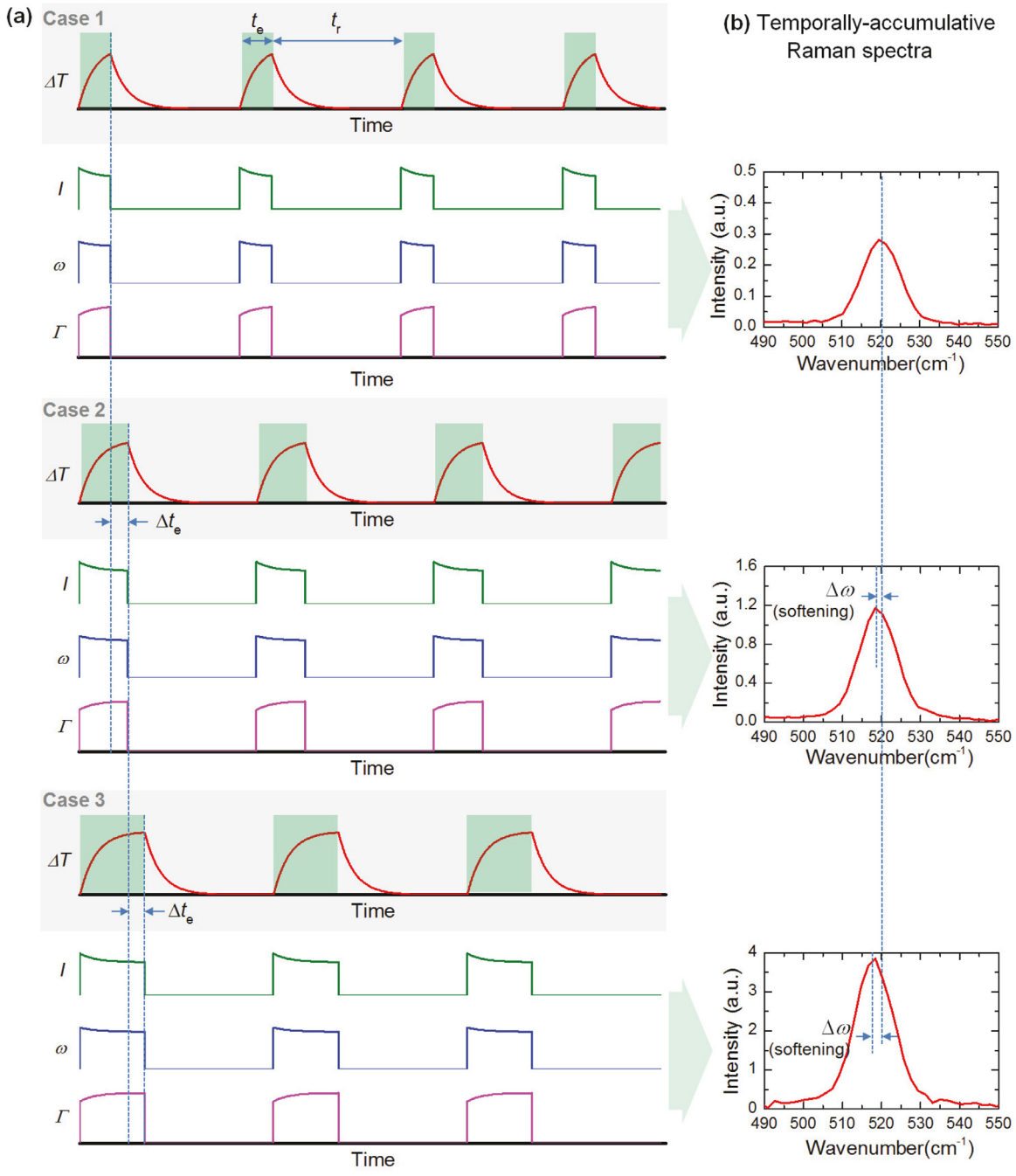


**Fig. 12.** Physical concept of time-domain differential Raman. (a) Timing profiles of the laser pulse and the temperature evolution, and instant changes of Raman peak intensity ($I$), peak shift ($\omega$) and linewidth ($\Gamma$). (b) The corresponding temporally accumulative Raman spectra of one cycle in three cases. (Reprinted from Ref. [14]. Reproduced with permission of Optical Society of America. All rights reserved)

gration time would be the same no matter how fast the laser is modulated. This helps a great deal to significantly weaken the disturbance from surroundings. This great advantage may improve the possible temporal resolution to faster than nanoseconds in Raman-based temperature response. Although both the TD-Raman and FR-Raman have been developed to measure the thermal diffusivity of materials at the micro/nanoscale, it should be able to probe the transient thermal response of two materials immediately next to each other because of its superior material-specific temperature measurement capacity. This will provide a great potential to directly measure the interface thermal conductance.

### 4.3. Laser flash Raman spectroscopy method

In Zhang's group, another powerful temporal Raman-based characterization method, named laser flash Raman spectroscopy method, has been well developed [12,13,16,23,87,102]. It has been further improved to a dual-wavelength laser flash Raman spectroscopy method [24] for wider applications. Liu *et al.* first developed the laser flash Raman spectroscopy method and applied this new method to measure the thermal properties for MWCNTs [13]. Instead of continuous wave laser heating, the laser flash Raman spectroscopy method employs a square pulsed laser to heat the sample as shown in Fig. 14. The laser flash Raman spectroscopy

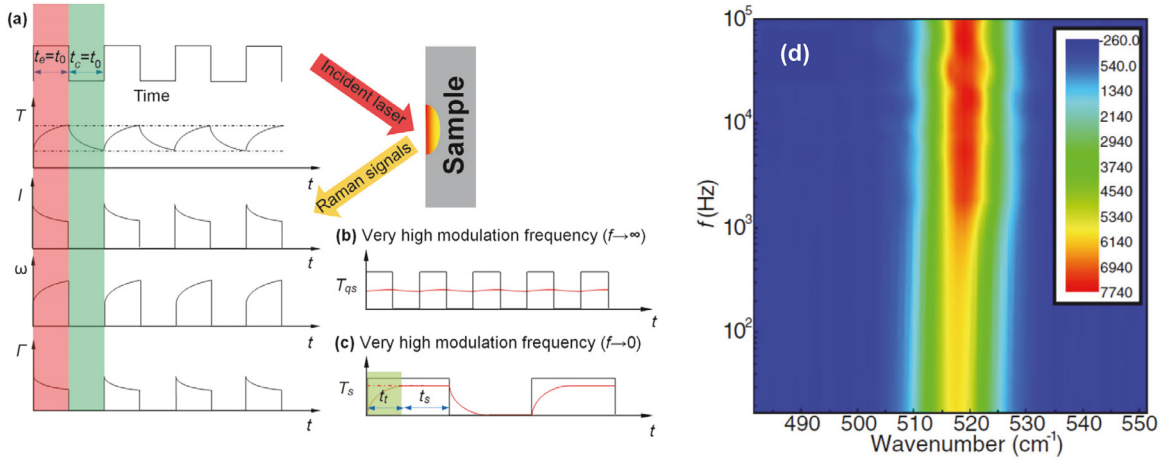


**Fig. 13.** Concept and physics of FR-Raman. (a) Timing profiles of the laser pulse and the temperature evolution, and instant changes of Raman peak intensity ($I$), shift ($\omega$) and linewidth ($\Gamma$). (b) The quasi-steady state at very high $f$. (c) The steady state at very low $f$. (d) Contour map of Si Raman peak intensity against the modulated frequency and Raman shifts. (Reprinted from Ref. [15]. Reproduced with permission of 2015 Optical Society of America. All rights reserved)

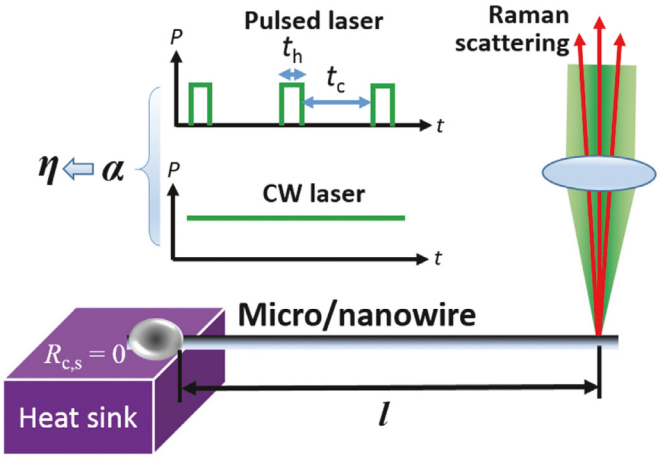


**Fig. 14.** Physical model of the laser-flash Raman method.(Reprinted from Ref. [87]. Reproduced with permission of Elsevier. All rights reserved)

shares the similar principle as the TD-Raman, and involves normalization to the steady-state Raman data. The sample experiences significant temperature rises during the heating period, and the heating period is short enough that no temperature rise exists at the far end away from the heating point. Then a long enough time interval between two pulses is applied to completely cool the sample down to the ambient temperature.

A physical model is developed to describe the average temperature rise along the length of the pulse duration over the irradiated area:

$$\bar{\theta}(0, 0 \sim \tau_h) = \frac{4\eta P_1 \sqrt{\alpha}}{3Ak\sqrt{\pi}} \sqrt{\tau_h}, \tag{11}$$

where $\bar{\theta}$ is the average temperature rise at the heating point, $\eta$ is the optical absorption coefficient, $P_1$ is the incident laser power in the pulsed measure, $\tau_h$ is the flash time. A, $k$, and $\alpha$ are the cross-section area, thermal conductivity, and thermal diffusivity of the sample. In the meantime, the Raman spectrum of the same sample in the steady-state Raman method, $\bar{\theta}(0) = \eta P_2 l/(kA)$, is obtained to normalize the transient Raman response, in order to eliminate the optical absorption coefficient $\eta$ and the unknown thermal conductivity $k$ of the sample. $P_2$ is the incident laser power in the CW laser measurement. By fitting the normalized temperature rise curve against the length of the pulse duration, the thermal diffusivity can be determined without knowing the optical absorption coefficient. Different from the steady-state Raman measurement where the accurate optical absorption is essential for thermal characterization, the laser flash Raman spectroscopy method calculates the thermal diffusivity through fitting the normalized temperature rise curve, the absolute laser heating level is not required.

Li *et al.* applied a "laser-flash Raman mapping" method to simultaneously measure the thermal contact resistance at the carbon fiber–carbon fiber junction and their thermal conductivities [87]. Laser is used to heat the sample and the laser absorptivity is experimentally determined by a transient laser-flash Raman technique. The laser heating position is changed along two connected carbon fibers, and the change of temperature rise with varying positions is in-situ measured from the temperature dependent Raman shifts. The high spatial resolution of the micro-Raman mapping allows direct observation of the abrupt jump of thermal resistance at the carbon fiber–carbon fiber junction, from which Li *et al.* extracted the thermal contact resistance as well as the thermal conductivity.

As shown in Fig. 15, the thermal conductivities of the individual carbon fibers are around 200 W/(m•K), and the thermal contact resistance of the carbon fiber–carbon fiber junction is $(2.98 \pm 0.92) \times 10^5$ K/W. That verified this method is a feasible non-contact measurement method for simultaneous characterization and manipulation of contact/interface heat conduction between various micro- and nano-fibers. Using the laser-flash Raman method, Li *et al.* also measured the thermal diffusivity and thermal conductivity of supported and suspended graphene [102] and the result is shown in Fig. 16.

As shown in Fig. 16, the thermal conductivity and thermal diffusivity were extracted by analytically fitting the temperature rise ratios as a function of spot size and pulse duration, respectively. The measured thermal conductivities were in the range of $0.84\times10^3$-$1.5\times10^3$ W/(m•K) and the measured thermal diffusivity is in the range of $5.3\times10^{-4}$-$6.8\times10^{-4}$ m$^2$/s. Furthermore, the specific heat of the measured graphene samples can be calculated as $C = k/\alpha\rho$, which is about 700 J/(kg•K). The value of specific heat agrees well with that of graphite.

### 4.4. Variable-spot-size laser flash Raman spectroscopy method

Due to the recent research [103] showing that local phonon non-equilibrium for samples with long phonon relaxation lengths measured in a highly focused laser spot using advanced Raman methods, the variable-spot-size laser-flash Raman method has

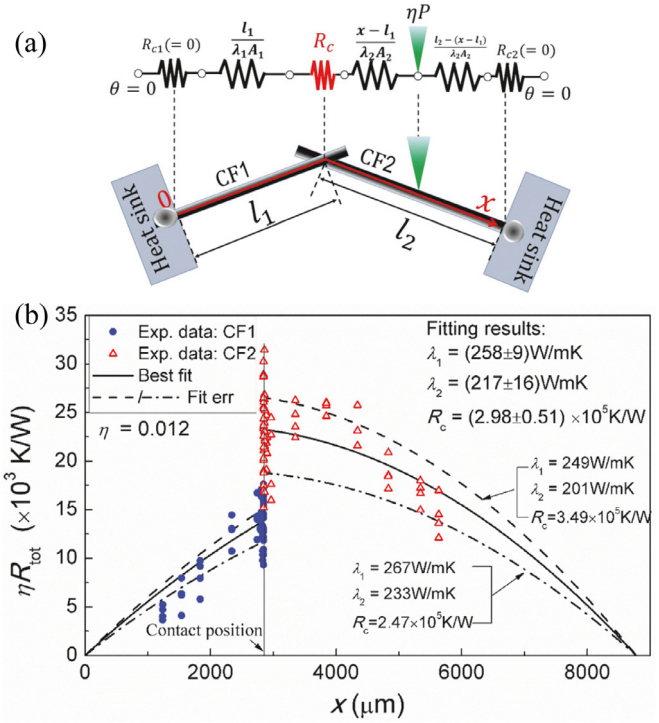


**Fig. 15.** (a) Mechanism of contact resistance measurement across the junction between two carbon fibers. (b) Measured thermal resistance distribution of the carbon fiber-carbon fiber sample and the best fit of the individual carbon fibers' thermal conductivities and thermal contact resistance of the carbon fiber–carbon fiber junction. (Reprinted from Ref. [87]. Reproduced with permission of Elsevier. All rights reserved)

been proposed. It can measure the thermal properties as well as the laser absorption in supported 2D van der Waals heterostructure with arbitrary layers as shown in Fig. 17. Li *et al.* established

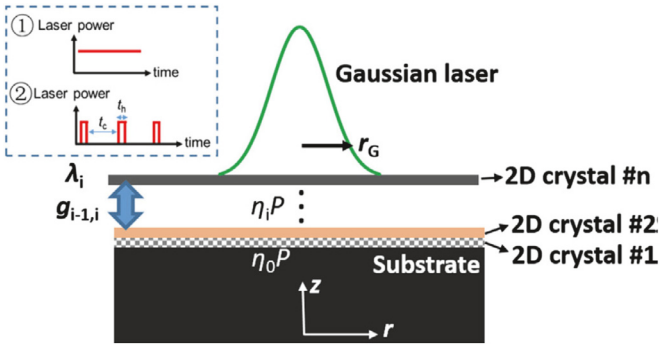


**Fig. 17.** Schematic of the heat conduction model for Gaussian laser heating substrate-supported n-layer 2D heterostructure. (Reprinted from Ref. [23]. Reproduced with permission of Elsevier. All rights reserved)

the heat conduction model of the supported 2D van der Waals heterostructure and analyzed the sensitivity and uncertainty for the multi-response multi-parameter [23]. Investigation of multiple steady-state and transient-state cases showed that the transient temperature curves are sensitive to the thermal properties. This variable-spot-size technique with submicron spot sizes is more applicable to 2D materials with short relaxation length, while a sufficient large spot is required for the samples with long relaxation length.

### 4.5. Dual-wavelength flash Raman spectroscopy method

The temporal resolutions of the laser flash Raman Spectroscopy method are still not satisfactory due to limits in the rising time of the electro-optical modulator (EOM) signal. For instance, the temperature rise of a supported carbon nanotube can approach steady state within 10 ns, while the highest reported temporal resolution of the transient Raman spectroscopy method is ~15 ns, so this method cannot be used with supported carbon nanotubes. To resolve this problem, Fan *et al.* proposed an in-situ

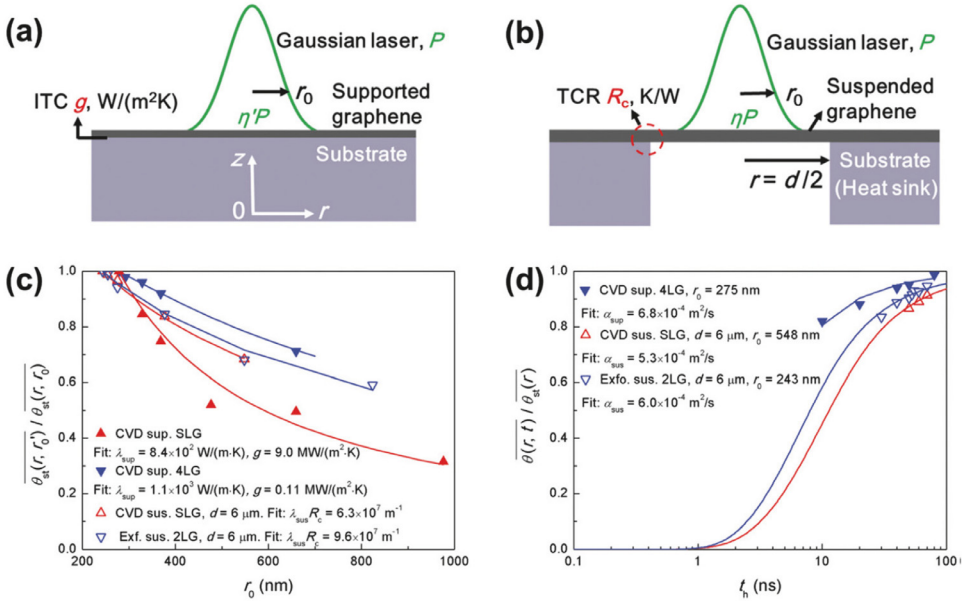


**Fig. 16.** Extraction of thermophysical properties from normalized temperature rise curves. (a) Schematic of the heat conduction model for supported graphene. (b) Schematic of the heat conduction model for circular suspended graphene. (c) Extraction of thermal conductivity $\lambda_{sup}$ and $g$ for the two supported graphene samples and ($\lambda_{sus}R_c$) for the two suspended graphene samples by the analytical fitting of the normalized temperature rise as a function of laser spot radius. (d) Extraction of thermal diffusivity of one supported and two suspended graphene samples by the analytical fitting of the normalized temperature rise as a function of laser pulse duration. The symbols and solid lines respectively represent the measured temperature rise ratios and the best fits to the experimental data. (Reprinted from Ref. [102]. Reproduced with permission of The Royal Society of Chemistry. All rights reserved)

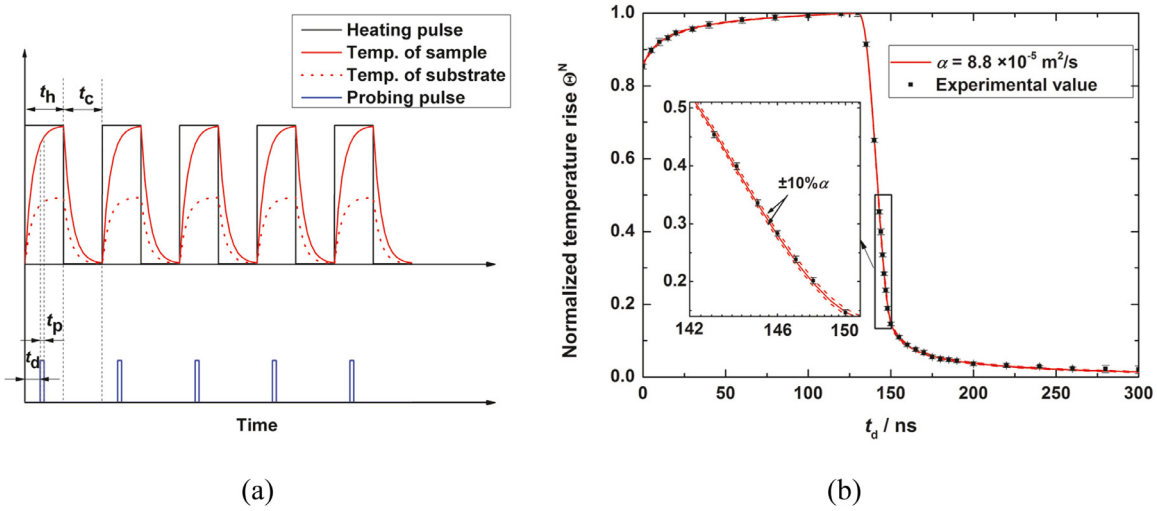


**Fig. 18.** (a) Measurement principle of the dual-wavelength laser flash Raman spectroscopy method. (b) Measured and best-fit normalized temperature rise of the silicon sample during heating and cooling. (Reprinted from Ref. [24]. Reproduced with permission of Springer Nature. All rights reserved)

"dual-wavelength laser flash Raman spectroscopy method" [24]. As shown in Fig. 18(a), in this method, a heating pulse is used to heat the sample and another pulsed laser with a different wavelength and negligible heating effect is employed as a probe to measure the sample temperature variation. The temperature rise and fall curves can be measured by changing the delay between the heating pulse and the probing pulse, and the thermal diffusivity of the sample can be characterized by fitting the temperature variation curves. The time delay between the heating and probing pulses can be precisely controlled with a minimum step of 100 ps so that the temperature variations can be scanned with an ultra-high temporal resolution of 100 ps. This is similar to the transient thermal reflectance concept used in the pump-probe technique. Fan *et al.* established a bulk material model to verify the measurement accuracy. Fig. 18(b) shows the measured thermal diffusivity of a silicon sample, which is $8.8\times10^{-5}$ m$^2$/s with a 3% difference between the measured value and the average result for bulk silicon in the literature.

Based on the dual-wavelength laser flash Raman spectroscopy principle, Hu *et al.* proposed a method for measuring supported 1-D nanowire, and then measured a supported silicon nanowire [106]. The temperature variations of single nanowire in the heating and cooling processes are shown in Fig. 19. The thermal diffusivity of silicon nanowire is calculated to be $8.3\times10^{-5}$ m$^2$/s. Furthermore, with the density and specific heat capacity of nanowire consistent with the bulk values [2.33 g/cm$^3$, 745 J/(kg•K)], the thermal conductivity can be determined with high accuracy. Finally, the best-fitted thermal conductivity is 145 W/(m•K) and the laser absorption is 6.6%. Meanwhile, the thermal resistance $R_c$ can be determined as 2.63 m•K/W.

The laser flash Raman spectroscopy method and its advanced methods utilize multiple laser sources to feasibly realize diverse thermal properties characterization in different nanostructures.

### *4.6. Dual-wavelength flash Raman spectroscopy mapping method*

As mentioned in Section 2.3, for normal Raman measurement, the spatial resolution of temperature measurement is limited by the size of the focused laser spot if the sample's size is larger than the laser spot size. Material control and optical field control can further enhance the spatial resolution. However, these control approaches are not suitable for all samples and will make the experiment more complicated. To simply enhance the spatial resolution and then further enhance the measurement sensitivity of the DFR method, Fan *et al.* further developed a DFR mapping method [24,25]. Using a fixed heating laser spot to heat the sample to induce a temperature distribution, then moving the position of the probing laser spot, the temperature variation curves at various positions can be measured, and the thermophysical properties can be then obtained. The spatial resolution of the center distance between heating and probing laser spots can reach 50 nm. As shown in Fig. 20, case analysis showed that the measurement sensitivity of this mapping method for nanofilm [25] and nanofiber [24] can be significantly enhanced compared with the concentric DFR method. Meanwhile, a temperature phase method was proposed to analyze the measured data, and the virtual experiments showed the measurement uncertainty of thermal diffusivity for suspended nanofilm can be better than 5% [25].

This method can also be used to determine the thermal diffusivity of 2D anisotropic materials [104]. The principal axis can be identified from a steady state temperature mapping as shown in Fig. 21, and the anisotropic thermal diffusivities can then be accurately extracted from transient temperature variation curves. This method is the only reported approach that can directly measure the thermal diffusivity of 2D anisotropic materials with thicknesses of $<$ 100 nm with an uncertainty less than 5%.

## 5. Energy Transport State-resolved Raman (ET-Raman): Down to ps Resolution and Probing of Conjugated Hot Carrier Diffusion

### *5.1. ET-Raman: ns and ps scale resolution*

In the abovementioned work, phonons are the main carriers for transferring thermal energy in materials. Most 2D atomic layer materials belong to the realm of semiconductor and they have band gaps. In Raman-based thermal measurements for the heat transfer process in 2D semiconductors, the photons of Raman excitation laser have a higher energy than the band gap, and will excite electron-hole pairs. The generated electrons then participate in transferring heat in materials. Thus, both electrons and phonons are main carriers contributing to the thermal energy transport in 2D materials. The heat transfer in 2D semiconductors supported on a substrate consists of three physical processes as shown in the Fig. 22 (a). First, as the incident photons arrive at the surface of 2D semiconductors, the 2D semiconductors absorb incident energy and the electron-hole pairs are excited and then generate hot carriers (free electrons) which will diffuse immediately in space and

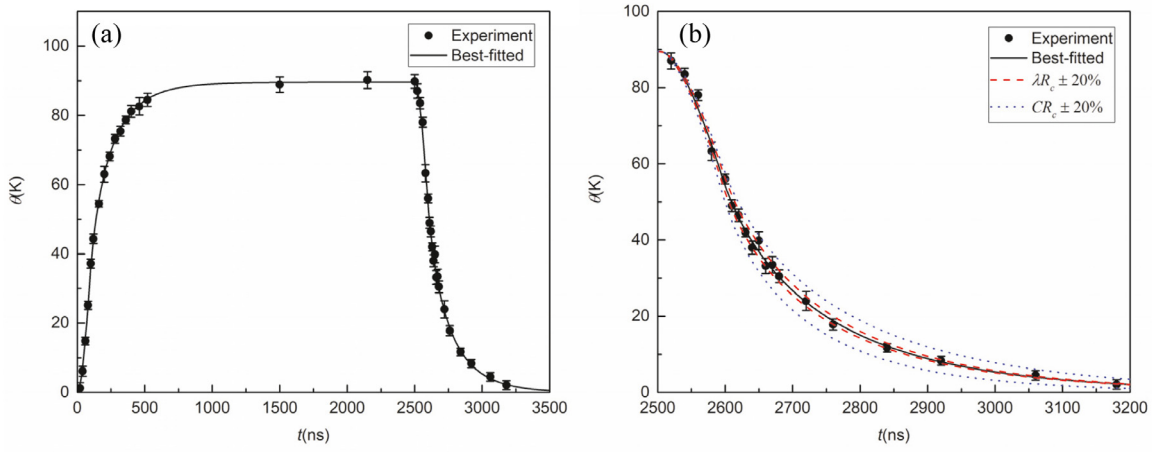


**Fig. 19.** Measured and best-fit normalized temperature rise of the supported silicon nanowire during heating and cooling. (Reprinted from Ref. [106]. Reproduced with permission of Elsevier. All rights reserved)

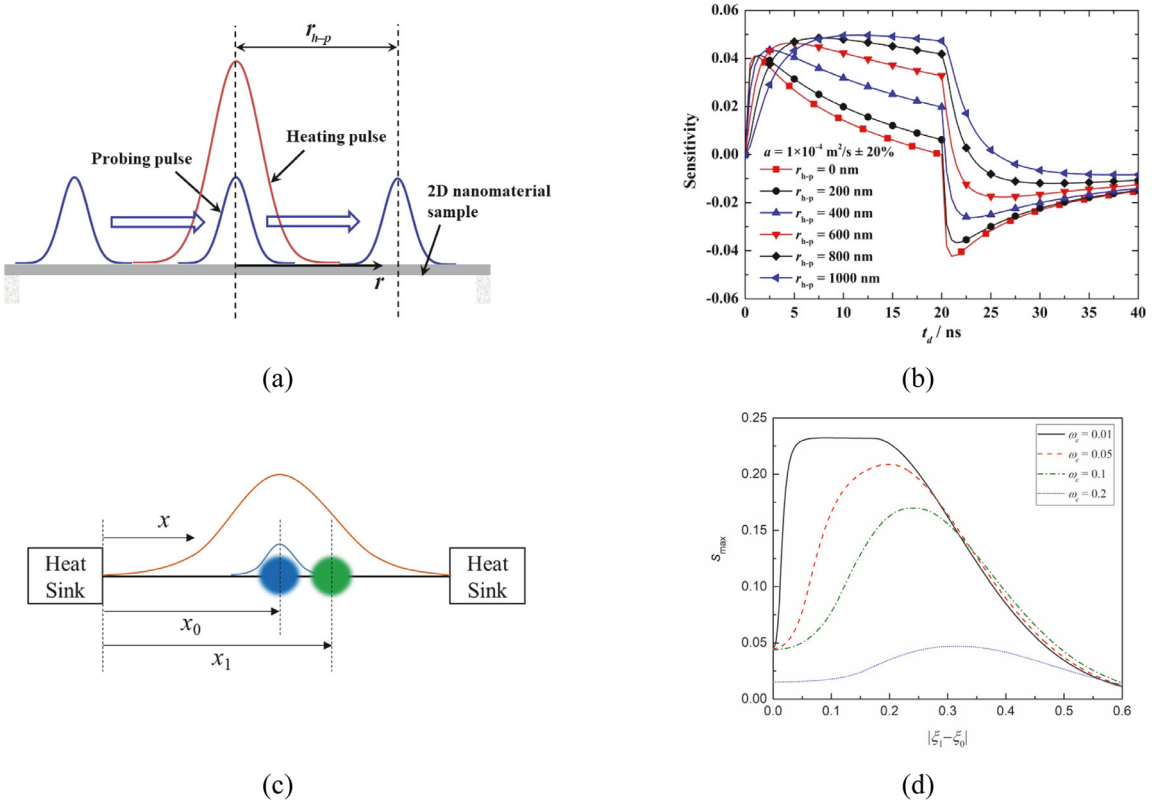


**Fig. 20.** (a) Schematic of the suspended nanofilm; (b) Sensitivity of nanofilm thermal diffusivity for various center distances between heating and probing laser spots; (c) Schematic of the suspended nanofiber; (d) Sensitivity of nanofiber thermal diffusivity for various center distances between heating and probing laser spots. (Reprinted from Ref. [24,25]. Reproduced with permission of Elsevier and Science China Press. All rights reserved)

recombine with holes at another place away from the heating area. This process can be analytically described as

$$D\nabla^2\Delta N - \frac{\Delta N}{\tau} + \frac{\partial n_0}{\partial T}\frac{\Delta T}{\tau} + \Phi\alpha = 0, \tag{12}$$

where $D$ ($cm^2\ s^{-1}$), $\tau$ (s) and $\Phi$ (photons per $cm^3$ per s) are the carrier diffusion coefficient, the electron-hole recombination time of the 2D semiconductor and the incident photon flux. $\alpha$ is the optical absorption coefficient of the 2D semiconductor.

The second process is that phonons obtain thermal energy from hot carriers and electron-hole recombination and transfer the energy to another place of lower energy. This process mainly happens in the in-plane and depends on the thermal conductivity of the 2D semiconductors. It has the following governing equation

$$k\nabla^2\Delta T + (h\nu - E_g)\Phi\alpha + E_g\frac{\Delta N}{\tau} = 0, \tag{13}$$

where $\Delta T(r,t)$ (K), $k$ [W/(m•K)] and Eg (eV) are the temperature rise, the thermal conductivity and the bandgap energy of the 2D

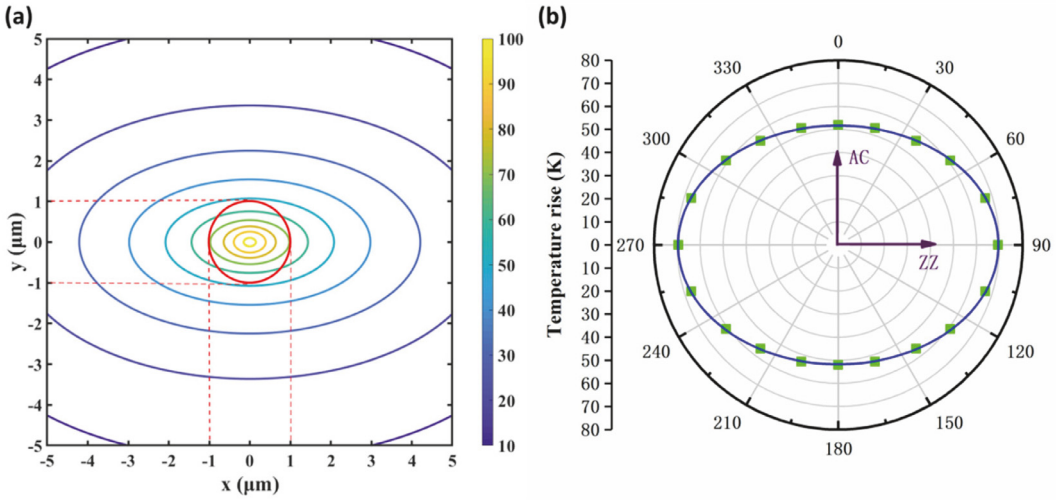


**Fig. 21.** (a) Steady in-plane temperature distribution in BP heated with a Gaussian laser. The 1 $\mu$m radius red circle represents the probe beam circumference. (b) The green dots are the temperatures at different positions along the probe circumference and the blue elliptical contour is the temperature fit in polar coordinates. (Reprinted from Ref. [104]. Reproduced with permission of Elsevier. All rights reserved)

semiconductor. The third process is heat transfer across the plane and obviously that interface thermal resistances will dominate this process. The heat transfer across the interface can be described conceptually as $\Delta q = A(T_{2D}\text{-}T_s)/R$, where $\Delta q$ is the net heat flow, $A$ is the heating area, and $R$ is the interface thermal resistance. It is important to note that $A$ may be larger than the irradiated area, since the hot-carrier-diffusion will enlarge the heating region.

The hot carrier is very important, but has not been considered before until recent pioneering work in Wang's lab [17-21]. They have combined the continuous wave Raman method and picosecond Raman method and developed an energy transport state resolved Raman (ET-Raman) to characterize these processes and measured the in-plane thermal conductivity, hot carrier mobility, and interface thermal conductance of supported $MoS_2$. In their work, they used a Raman system with an excitation laser of 532 nm wavelength (2.33 eV), that is higher than the band gap of $MoS_2$ of 1.8eV-1.29eV [92,105] and can excite the hot electron-hole pairs.

In the picosecond Raman measurement showed in Figs. 22(d)-(f), since the pulse of the excited/heating laser is so short ($\sim$ 13 ps) that the thermal diffusion lengths of both $MoS_2$ and the substrate are shorter than the diameter of the dimension of the irradiated area. The temperature rise is mostly determined by the specific heat of the sample and substrate. In contrast, when using the continuous wave Raman method in Figs. 22(d)-(f), the heating time is long enough that heat transfer in both in-plane and cross-plane directions occur and reach steady state. By varying the size of the irradiated spot, the contributions of in-plane and cross-plane heat transfer and hot carrier diffusion to the total energy transport can be differentiated. For instance, when the laser spot is very large (e.g. under 20$\times$ objective), the 2D material's temperature rise is mostly determined by the interface thermal resistance. When the laser spot size is very small (e.g. under 100$\times$ objective), the in-plane heat conduction and hot carrier diffusion play more important roles in the measured temperature rise/Raman response.

A parameter termed Raman shift power coefficient (RSC) is then proposed and has an expression as $\chi = \partial\omega/\partial P$. It is determined by $k$, $D$, $R$, and laser absorption coefficient, and temperature coefficient of Raman shift. With the different states in Figs. 22 (b-f), five different $\chi$ can be obtained and based on them, three new normalized RSCs are then determined: $\Theta_n = \chi_{cw,n}/(\chi_{ps1} - \chi_{ps2})$, n = 1, 2, and 3. The term $\chi_{ps1} - \chi_{ps2}$ is from picosecond Raman and used to eliminate steady-state heat accumulation in the supported 2D semiconductor. The laser absorption coefficient and temperature coefficient of Raman shift are eliminated in $\Theta$, and make it only depend on $k$, $D$, and $R$.

Since there were three variables, ($k$, $D$, and $R$, and correspondingly, three $\Theta$'s), the regular data fitting was hard to perform for this case. A 3D theoretical model was built to simulate the temperature rise in the $MoS_2$ sample in the experiment. Statistically, the normalized probability distribution function, $\Omega_i = \exp[-(\Theta_i - \Theta_{exp\_i})^2/(2\sigma_i)^2]$, was employed to describe the precision of $k$, $D$, and $R$. $\Theta_i$ and $\Theta_{exp\_i}$ are the normalized RSC from simulation and experiment, and $i$ = 1, 2, 3 denotes $k$, $D$, and $R$, respectively. $\sigma_i$ is the uncertainty of the experiment. The combined influence of three variables was written as $\Omega$ ($k$, $D$, $R$) = $\Omega_1 \bullet \Omega_2 \bullet \Omega_3$. The best set of the interface resistance, hot carrier mobility, and in-plane thermal conductivity of the sample could be determined when $\Omega$ ($k$, $D$, $R$) equals one. That means that the theoretical result agreed with the experimental result to the best. Fig. 23 shows the process of determining $k$, $D$, and $R$. Based on this energy-resolved Raman technique, the complex energy transport process in the 2D semiconductors has been revealed to the highest extent to date.

### 5.2. Frequency-domain energy transport state resolved ET-Raman (FET-Raman)

Zobeiri *et al.* took one more step forward to develop a Frequency domain Energy Transport state-resolved Raman (FET-Raman) on the basis of FR-Raman and ET Raman, aiming at investigating the thermal energy transport in the in-plane direction of suspended 2-D materials. It employed a CW laser and a modulator instead of two different laser sources as the heating source and Raman excitation source. Fig. 24 shows the detailed mechanism of in-plane thermal conductivity measurement using FET-Raman. First, the CW laser was applied to heat a suspended sample to various thermally steady-states at accordingly different laser power levels. RSC of the steady-state case ($\psi_{cw}$) had the expression of $\psi_{cw} = \partial\omega/\partial P \propto \alpha(\partial\omega/\partial T)/k$, where $k$ is the in-plane thermal conductivity of the sample, $\alpha$ is the laser absorption coefficient, and $\partial\omega/\partial T$ is the temperature coefficient of shift. However, it still needs $\alpha$ and $\partial\omega/\partial T$ calibration to determine $k$ with only steady state measurement. The frequency-resolved states were further employed to eliminate $\alpha$ and $\partial\omega/\partial T$.

In the frequency resolved cases, the CW laser was modulated to be a pulsed laser with equal on and off duration as

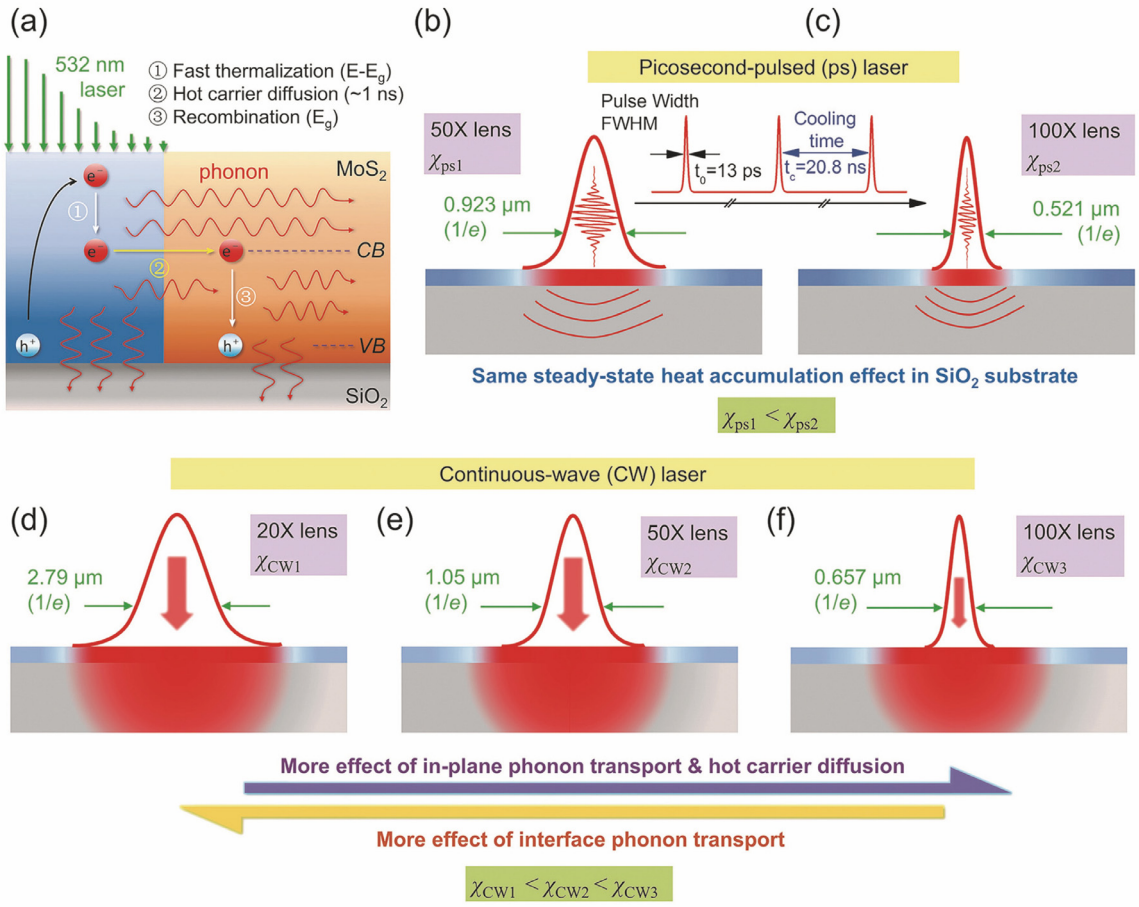


**Fig. 22.** The physical concept of five-state picosecond ET-Raman technique. (a) The generation, diffusion, and recombination of hot carriers in $MoS_2$ upon laser illumination (not to scale). (b) and (c) Laser heating in ps domain with weak heat transfer under 50× (b) and 100× (c) objectives. (b–f) CW laser heating with simultaneous heat transfer under 20× (d), 50× (e), and 100× (f) objectives to achieve different laser spot size heating to differentiate the effects of *R*, *k*, and *D*. (Reproduced from Ref. [21] with permission from the PCCP Owner Societies.)

shown in Figs. 24 (c) and (d). In the laser-on period, the incident laser heated the sample to raise its temperature, while during the laser-off period, the thermal energy dissipated to in and cross the plane of the sample and its temperature cooled down. Two typical heating states exist in frequency-resolved measurement shown in Figs. 24 (e) and (f). One is heating the sample at a very high frequency and the sample cannot reach the thermal steady state temperature, but a temperature at quasi-steady state which was termed in FR-Raman and readily proved to be half of the steady state temperature at the same incident power before modulation [15]. The other heating state is with very low frequency. The sample has a long enough time to reach the thermally steady-state during each laser-on period and also a long enough cooling time to cool down to room temperature thereafter in the laser-off period. However, the frequency-resolved measurement was achieved by selecting one appropriate frequency in middle of the frequency range from quasi-steady state to steady state. The obtained RSC in frequency-resolved case $\psi_{fr}$ is proportional to $\alpha(\partial\omega/\partial T)/(\rho c_p)f(k/\rho c_p)$. Thus, the value of $\psi_{cw}/\psi_{fr}$termed as normalized RSC is equal to $\kappa/(\rho c_p)f(k/\rho c_p)$. From this correlation, it is clear that the normalized RSC could exclude the effect of the accuracy of the laser absorption coefficient and Raman temperature coefficient, and is only dependent on the thermal conductivity when the volumetric heat capacity is assumed to be a constant in a small temperature rising process.

A 3D heat conduction model was built in Zobeiri's work to simulate the temperature rise in the abovementioned two measurement cases, and to further define the correlation between the normalized RSC and thermal conductivity. In the simulation, the laser absorption coefficient, incident power and the cross-plane thermal conductivity were arbitrarily selected as their effects on the normalized RSC were eliminated in the normalization. The author used a 36 nm-thick suspended $MoSe_2$ film as a sample, and the simulation result was shown in Fig. 25. Figs. 25 (a1)-(g1) show the temperature evolution and distribution in the sample, while the steady-state temperature distribution at the surface and in the cross-plane are illustrated in Figs. 25 (h1) and (h2).

Given that Raman signals are accumulated result over a space domain and a time span under laser irradiation, the concept of the average temperature was introduced in processing simulated results. For the steady-state case, the average temperature is $\bar{T}_{cw} = \int_0^{V_0} Ie^{-z/\tau_L}Td\nu/\int_0^{V_0} Ie^{-z/\tau_L}d\nu$, where $I$ is the laser intensity, $T$ is the temperature of each point of the sample, and $\tau_L$ is the optical absorption length at the wavelength of incident laser. In the measurement under a modulated laser, analogous to the steady-state case, the average temperature can be expressed as $\bar{T}_{fr} = \int_0^t\int_0^{V_0} Ie^{-z/\tau_L}Td\nu dt/\int_0^t\int_0^{V_0} Ie^{-z/\tau_L}d\nu dt$. After this averaging process, the theoretical normalized RSC with the definition of the ratio of $\bar{T}_{cw}$ to $\bar{T}_{fr}$ was simulated for different in-plane thermal conductivities of the sample. Compared with the experimental result to the theoretical curve of the normalized RSC against $k$, the in-plane thermal conductivity of the sample is finally determined. Using this method, Zobeiri, *et al.* has successfully measured the

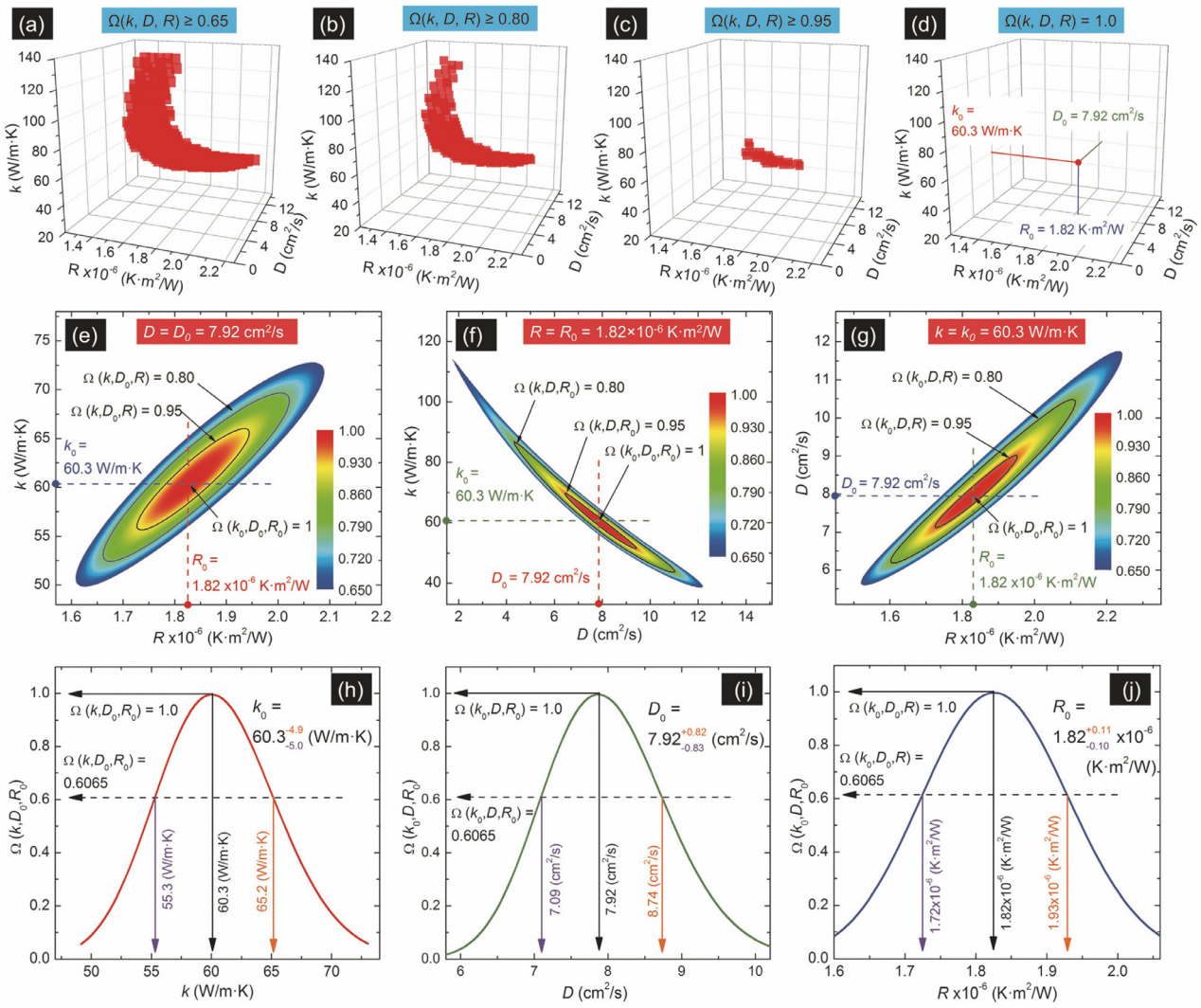


**Fig. 23.** Simultaneous determination of $k$, $D$, and $R$ of 2.4 nm-thick $MoS_2$ sample. (a–d) the evolution of distribution of Ω ($k$, $D$, $R$), when its value is increasing from 0.65 to 1. (e–g) The 2D contours of cross-sectional views of Ω ($k$, $D$, $R$) across the point of Ω ($k$, $D$, $R$) = 1 in (a) in three directions. (h–j) The determination of the uncertainty in $k$, $D$, and $R$. (Reproduced from Ref. [21] with permission from the PCCP Owner Societies.)

in-plane thermal conductivity of suspended $MoSe_2$ with different thicknesses: it increases from 6.2 ± 0.9 to 25.7 ± 7.7 W/(m•K), as its thickness changes from 5 nm to 80 nm.

The FET-Raman has been developed to investigate the in-plane heat transfer of suspended 2D materials. Similar to the laser flash Raman spectroscopy method, it employs two states, transient state and steady state, to eliminate the unknown laser absorption and temperature coefficients of Raman properties. However, different experimental procedures introduce differences into two physical models. In the laser flash Raman spectroscopy method, the pulsed laser in transient case had a short laser on duration and a long laser off duration in each period, so the sample could return to the original temperature after pulsed laser heating [12,13,102]. In contrast, in FET-Raman, the laser on and off durations are equal, and the sample could not totally cool down before the next pulse comes in. Then the quasi-steady-state and half of the temperature rise at steady state are utilized to account for this situation.

The physical models of two methods also show the different dependencies on thermal properties of the sample. In the laser flash Raman method, the temperature rise ratio of the transient state to steady state is applied and relies on the unknown properties of in-plane thermal conductivity, thermal diffusivity, and the thermal contract resistance between the sample layer and the heat sink. The controllable parameters of the radius of the laser spot were varied to extract those unknown thermal properties. Compared with the laser flash method, the physical model in FET-Raman was simplified by assuming the volumetric heat capacity of the sample layer to be constant in the measurement. The normalized RSC only depends on the in-plane thermal conductivity of the sample layer. By varying the incident power, the in-plane thermal conductivity of the sample was determined. Both methods have successfully measured the in-plane thermal conductivity of suspended 2D material layer, though different emphases are considered on the heat conduction model development and experimental measure.

## 6. Concluding Remarks

The recent advancements in Raman spectroscopy methods were critically reviewed for temperature and thermal properties measurements. The intrinsic properties of Raman peaks, including Raman shift, linewidth, and intensity, show good temperature responses with different sensitivities, and deconjugation of the correlations among these properties can reveal the effects of ther-

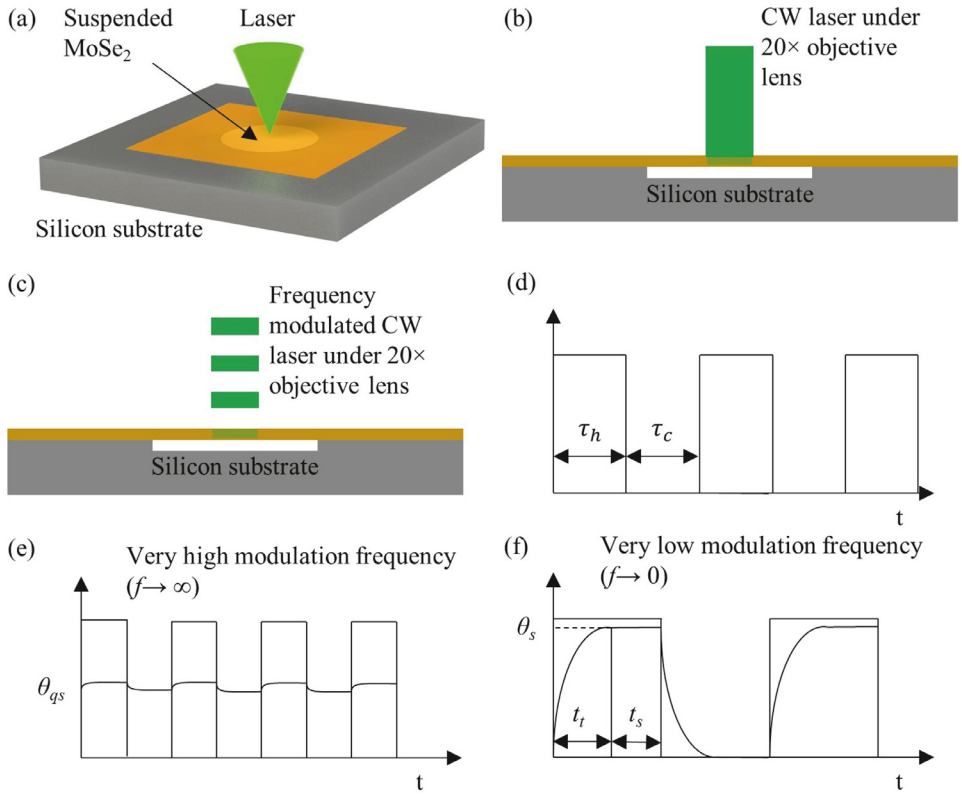


**Fig. 24.** Physical concept of Frequency-domain Energy Transport state-resolved Raman (FET-Raman) method. (a) A $MoSe_2$ nanosheet is suspended on a silicon substrate with a circular hole and irradiated with a 532 nm CW laser (b) and a 532 nm frequency-modulated laser (c). Temporal profiling of square-wave modulation of the laser (d). Theoretical temperature evolutions of the sample under very high modulation frequency (e) and under very low modulation frequency (f). (Reprinted from Ref. [22]. Reproduced with permission of Elsevier. All rights reserved)

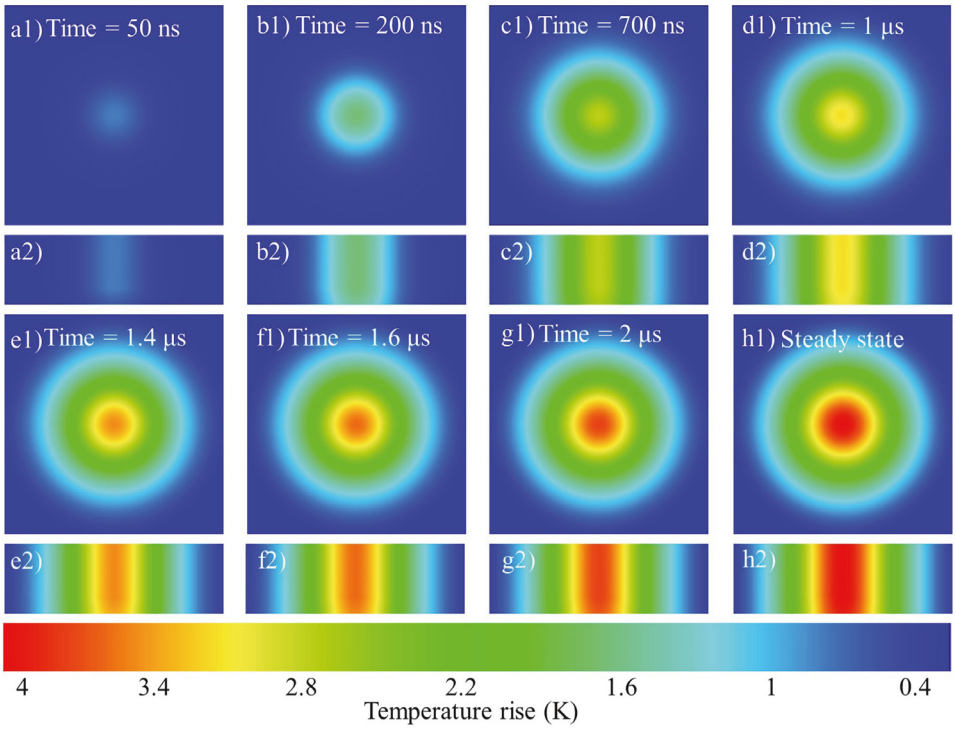


**Fig. 25.** Contour map of the temperature rise of the 36 nm $MoSe_2$ sample under laser irradiation as a function of time. The total heating time is 5 $\mu$s. (a1–h1) show the evolution of temperature rise of the sample top (10 $\mu$m × 10 $\mu$m). Figs. a2–h2 show the temperature rise of the sample side (cross-section view, 10 $\mu$m wide × 36 nm high). (Reprinted from Ref. [22]. Reproduced with permission of Elsevier. All rights reserved)

mal stress, interface optical interference, and optical focusing on the measured temperatures. Other sources of errors in the steady state Raman method are from the accuracy in the temperature coefficient calibration for Raman properties and the heating level evaluation. Different scenarios in temperature coefficients calibration and real measurement situation have been experimentally observed. The heating power and temperature rise should be kept as low as possible to minimize the errors in measurement. For heating level examination, large errors may arise when using optical properties from references due to structure difference from one sample to another. Alternatively, the feasibility of the temporal Raman methods demonstrates excellent performance of avoiding these errors as they are eliminated in the physical models. They provide a more efficient way for thermal properties determination with high accuracy.

However, the signal accumulation in Raman spectroscopy lowers the sensitivity of temperature probing in both time and space domains. To improve the resolution in both domains remains a theoretical and technical challenge. With the help of temporal Raman methods, the time resolution can be improved to picoseconds. Furthermore, taking advantage of both steady-state and transient Raman methods, the hot electron-hole pairs' generation and their contribution to heat transfer has been decomposed and deeply investigated in 2D semiconductors. Also, preliminary scanning Raman measurement has been performed to study the interface. To extend the capability of Raman method, the scanning application should be developed in future for the study of complexity in nanomaterials, since the Raman-based methods mainly study the thermal properties under or near the radiated area and the samples were usually assumed to have a uniform thermal property in- or cross-plane. Also, based on its noncontact feature, it is possible to apply these advanced Raman methods using an environment chamber to investigate the thermal properties over a wide temperature range.

## Declaration of competing interest

The authors declare that they have no known competing financial interests or personal relationships that could have appeared to influence the work reported in this paper.

## Acknowledgement

Support of this work by US National Science Foundation (CBET1930866), National Natural Science Foundation of China (Grant Nos. 51636002, 51827807), Science Fund for Creative Research Groups (No. 51621062), Program for Professor of Special Appointment (Eastern Scholar) at Shanghai Institutions of Higher Learning, and China Scholarship Council is gratefully acknowledged.

## Supplementary materials

Supplementary material associated with this article can be found, in the online version, at doi:10.1016/j.ijheatmasstransfer.2020.119751.

## References

[1] C. Kittel, Introduction to Solid State Physics, Wiley, New York, 2004.
[2] B. Attal-Trétout, P. Bouchardy, P. Magre, M. Péalat, J.P. Taran, CARS in combustion: Prospects and problems, Applied Physics B 51 (1) (1990) 17–24.
[3] D.C.B. Harris, M.D, Symmetry and spectroscopy: An Introduction to Vibrational and Electronic Spectroscopy, 1st ed., Oxford University Press, New York, USA, 1978.
[4] R.S. Das, Y.K. Agrawal, Raman spectroscopy, Recent advancements, techniques and applications, Vibrational Spectroscopy 57 (2) (2011) 163–176.
[5] P.R.N. Childs, J.R. Greenwood, C.A. Long, Review of temperature measurement, Review of Scientific Instruments 71 (8) (2000) 2959–2978.
[6] Z. Xu, Z. He, S. Ying, F. Xiu, F. Fang, Topic review, Application of Raman spectroscopy characterization in micro/nano-machining, Micromachines 9 (7) (2018) 361.
[7] T. Beechem, S. Graham, Temperature Measurement of Microdevices using Thermoreflectance and Raman Thermometry, in: P.J. Hesketh (Ed.), Bio-NanoFluidic MEMS, Springer, US: Boston, MA, 2008, pp. 153–174.
[8] Y. Yue, J. Zhang, X. Wang, Micro/nanoscale spatial resolution temperature probing for the interfacial thermal characterization of epitaxial graphene on 4H-SiC, Small 7 (23) (2011) 3324–3333.
[9] X. Tang, S. Xu, X. Wang, Thermal probing in single microparticle and microfiber induced near-field laser focusing, Optics Express 21 (12) (2013) 14303–14315.
[10] X. Tang, S. Xu, X. Wang, Corrugated epitaxial graphene/SiC interfaces: photon excitation and probing, Nanoscale 6 (15) (2014) 8822–8830.
[11] X. Tang, S. Xu, J. Zhang, X. Wang, Five orders of magnitude reduction in energy coupling across corrugated graphene/substrate interfaces, ACS Applied Materials&Interfaces 6 (4) (2014) 2809–2818.
[12] Q. Li, X. Zhang, Y. Hu, Laser flash Raman spectroscopy method for thermophysical characterization of 2D nanomaterials, Thermochimica Acta 592 (2014) 67–72.
[13] J. Liu, H. Wang, Y. Hu, W. Ma, X. Zhang, Laser flash-Raman spectroscopy method for the measurement of the thermal properties of micro/nano wires, Review of Scientific Instruments 86 (1) (2015) 014901.
[14] S. Xu, T. Wang, D.H. Hurley, Y. Yue, X. Wang, Development of time-domain differential Raman for transient thermal probing of materials, Optics Express 23 (8) (2015) 10040–10056.
[15] T. Wang, S. Xu, D.H. Hurley, Y. Yue, X. Wang, Frequency-resolved Raman for transient thermal probing and thermal diffusivity measurement, Optics Letters 41 (1) (2016) 80–83.
[16] Q. Li, W. Ma, X. Zhang, Laser flash Raman spectroscopy method for characterizing thermal diffusivity of supported 2D nanomaterials, International Journal of Heat and Mass Transfer 95 (2016) 956–963.
[17] P. Yuan, C. Li, S. Xu, J. Liu, X. Wang, Interfacial thermal conductance between few to tens of layered-$MoS_2$ and c-Si: Effect of $MoS_2$ thickness, Acta Materialia 122 (2017) 152–165.
[18] P. Yuan, J. Liu, R. Wang, X. Wang, The hot carrier diffusion coefficient of sub-10 nm virgin $MoS_2$: uncovered by non-contact optical probing, Nanoscale 9 (20) (2017) 6808–6820.
[19] P. Yuan, H. Tan, R. Wang, T. Wang, X. Wang, Very fast hot carrier diffusion in unconstrained $MoS_2$ on a glass substrate: discovered by picosecond ET-Raman, RSC Advances 8 (23) (2018) 12767–12778.
[20] P. Yuan, R. Wang, H. Tan, T. Wang, X. Wang, Energy Transport State Resolved Raman for Probing Interface Energy Transport and Hot Carrier Diffusion in Few-Layered $MoS_2$, ACS Photonics 4 (12) (2017) 3115–3129.
[21] P. Yuan, R. Wang, T. Wang, X. Wang, Y. Xie, Nonmonotonic thickness-dependence of in-plane thermal conductivity of few-layered $MoS_2$: 2.4 to 37.8 nm, Phys Chem Chem Phys 20 (40) (2018) 25752–25761.
[22] H. Zobeiri, R. Wang, T. Wang, H. Lin, C. Deng, X. Wang, Frequency-domain energy transport state-resolved Raman for measuring the thermal conductivity of suspended nm-thick $MoSe_2$, International Journal of Heat and Mass Transfer 133 (2019) 1074–1085.
[23] Q. Li, X. Zhang, K. Takahashi, Variable-spot-size laser-flash Raman method to measure in-plane and interfacial thermal properties of 2D van der Waals heterostructures, International Journal of Heat and Mass Transfer 125 (2018) 1230–1239.
[24] A. Fan, Y. Hu, W. Ma, H. Wang, X. Zhang, Dual-wavelength laser flash raman spectroscopy method for in-situ measurements of the thermal diffusivity: principle and experimental verification, Journal of Thermal Science (2019) 159–168.
[25] A.R. Fan, Y.D. Hu, H.D. Wang, W.G. Ma, X. Zhang, Dual-wavelength flash Raman mapping method for measuring thermal diffusivity of suspended 2D nanomaterials, International Journal of Heat and Mass Transfer 143 (2019) 118460.
[26] J. Wu, M. Lin, X. Cong, H. Liu, P. Tan, Raman spectroscopy of graphene-based materials and its applications in related devices, Chemical Society Reviews 47 (5) (2018) 1822–1873.
[27] A. Polman, H.A. Atwater, Photonic design principles for ultrahigh-efficiency photovoltaics, Nature Materials 11 (2012) 174.
[28] I. Jo, M.T. Pettes, E. Ou, W. Wu, L. Shi, Basal-plane thermal conductivity of few-layer molybdenum disulfide, Applied Physics Letters 104 (20) (2014) 201902.
[29] J. Liu, G.-M. Choi, D.G. Cahill, Measurement of the anisotropic thermal conductivity of molybdenum disulfide by the time-resolved magneto-optic Kerr effect, Journal of Applied Physics 116 (23) (2014) 233107.
[30] S. Sahoo, A.P.S. Gaur, M. Ahmadi, M.J.F. Guinel, R.S. Katiyar, Temperature-dependent Raman Studies and Thermal Conductivity of Few-Layer $MoS_2$, The Journal of Physical Chemistry C 117 (17) (2013) 9042–9047.
[31] E. Pop, Energy dissipation and transport in nanoscale devices, Nano Research 3 (3) (2010) 147–169.
[32] R.F. Wallis, M. Balkanski, Many-Body Aspects of Solid State Spectroscopy, North-Holland Physics, Amsterdam, 1986.
[33] W.H. Weber, Raman Scattering in Materials Science, Springer, New York, 2000.
[34] T.R. Hart, R.L. Aggarwal, B. Lax, Temperature dependence of raman scattering in silicon, Physical Review B 1 (2) (1970) 638–641.
[35] R.M. Dickson, A.B. Cubitt, R.Y. Tsien, W.E. Moerner, On/off blinking and

switching behaviour of single molecules of green fluorescent protein, Nature 388 (6640) (1997) 355–358.
[36] W.E. Moerner, M. Orrit, Illuminating single molecules in condensed matter, Science 283 (5408) (1999) 1670–1676.
[37] J. Zhou, Y. Hui, Y. Zheng, H. Wu, Highly fluorescent poly(dimethylsiloxane) for on-chip temperature measurements, Advanced Functional Materials 19 (2) (2010) 324–329.
[38] L. Gui, C.L. Ren, Temperature measurement in microfluidic chips using photobleaching of a fluorescent thin film, Applied Physics Letters 92 (2) (2008) 024102.
[39] A. Zolfaghari, T. Chen, A.Y. Yi, Additive manufacturing of precision optics at micro and nanoscale, International Journal of Extreme Manufacturing 1 (1) (2019) 012005.
[40] C.P. Grigoropoulos, Laser synthesis and functionalization of nanostructures, International Journal of Extreme Manufacturing 1 (1) (2019) 012002.
[41] J. Dakin, D. Pratt, G. Bibby, J. Ross, Distributed optical fibre Raman temperature sensor using a semiconductor light source and detector, Electronics Letters 21 (13) (1985) 569–570.
[42] J. Cui, K. Amtmann, J. Ristein, L. Ley, Noncontact temperature measurements of diamond by Raman scattering spectroscopy, Journal of Applied Physics 83 (12) (1998) 7929–7933.
[43] H. Lo, A. Compaan, Raman measurement of lattice temperature during pulsed laser heating of silicon, Physical Review Letters 44 (24) (1980) 1604.
[44] G. Vaughan, D. Wareing, S. Pepler, L. Thomas, V. Mitev, Atmospheric temperature measurements made by rotational Raman scattering, Applied Optics 32 (15) (1993) 2758–2764.
[45] M.S. Liu, L.A. Bursill, S. Prawer, R. Beserman, Temperature dependence of the first-order Raman phonon line of diamond, Physical Review B 61 (5) (2000) 3391.
[46] R. Cuscó, E. Alarcón-Lladó, J. Ibanez, L. Artús, J. Jimenez, B. Wang, M.J. Callahan, Temperature dependence of Raman scattering in ZnO, Physical Review B 75 (16) (2007) 165202.
[47] I. Calizo, A.A. Balandin, W. Bao, F. Miao, C.N. Lau, Temperature dependence of the Raman spectra of graphene and graphene multilayers, Nano Letters 7 (9) (2007) 2645–2649.
[48] Y. Yue, X. Chen, X. Wang, Noncontact sub-10 nm temperature measurement in near-field laser heating, ACS Nano 5 (6) (2011) 4466.
[49] A. Campion, P. Kambhampati, Surface-enhanced Raman scattering, Chemical society reviews 27 (4) (1998) 241–250.
[50] R.M. Stockle, Y.D. Suh, V. Deckert, R. Zenobi, Nanoscale chemical analysis by tip-enhanced Raman spectroscopy, Chemical Physics Letters 318 (1-3) (2000) 131–136.
[51] S. Nie, S.R. Emory, Probing single molecules and single nanoparticles by surface-enhanced Raman scattering, science 275 (5303) (1997) 1102–1106.
[52] B. Pettinger, B. Ren, G. Picardi, R. Schuster, G. Ertl, Nanoscale probing of adsorbed species by tip-enhanced Raman spectroscopy, Physical Review Letters 92 (9) (2004) 096101.
[53] X. Tang, S. Xu, X. Wang, Nanoscale probing of thermal, stress, and optical fields under near-field laser heating, Plos One 8 (3) (2013) e58030.
[54] R.C. Maher, Cohen, L.F. Etchegoin, P. Hartigan, H.J.N. Brown, R.J.C., M.J.T. Milton, Stokes/anti-Stokes anomalies under surface enhanced Raman scattering conditions, The Journal of chemical physics 120 (24) (2004) 11746–11753.
[55] F. Pozzi, J.R. Lombardi, S. Bruni, M. Leona, Sample treatment considerations in the analysis of organic colorants by surface-enhanced Raman scattering, Analytical Chemistry 84 (8) (2012) 3751–3757.
[56] M.V. Balois, N. Hayazawa, F.C. Catalan, S. Kawata, T.-a. Yano, T. Hayashi, Tip-enhanced THz Raman spectroscopy for local temperature determination at the nanoscale, Analytical and bioanalytical chemistry 407 (27) (2015) 8205–8213.
[57] K.-D. Park, E.A. Muller, V. Kravtsov, P.M. Sass, J. Dreyer, J.M. Atkin, M.B. Raschke, Variable-temperature tip-enhanced Raman spectroscopy of single-molecule fluctuations and dynamics, Nano letters 16 (1) (2015) 479–487.
[58] S. Webster, D.N. Batchelder, D.A. Smith, Submicron resolution measurement of stress in silicon by near-field Raman spectroscopy, Applied Physics Letters 72 (12) (1998) 1478–1480.
[59] Z. Ni, T. Yu, Y. Lu, Y. Wang, Y. Feng, Z. Shen, Uniaxial Strain on Graphene: Raman Spectroscopy Study and Band-Gap Opening, ACS Nano 2 (11) (2008) 2301–2305.
[60] F. Guinea, M.I. Katsnelson, A.K. Geim, Energy gaps and a zero-field quantum Hall effect in graphene by strain engineering, Nature Physics 6 (1) (2009) 30–33.
[61] T. Beechem, S. Graham, S.P. Kearney, L.M. Phinney, J.R. Serrano, Invited Article, Simultaneous mapping of temperature and stress in microdevices using micro-Raman spectroscopy, Rev Sci Instrum 78 (6) (2007) 061301.
[62] S. Xu, X. Tang, Y. Yue, X. Wang, Sub-micron imaging of sub-surface nanocrystalline structure in silicon, Journal of Raman Spectroscopy 44 (11) (2013) 1523–1528.
[63] Z.L. Wang, D.W. Tang, Investigation of heat transfer around microwire in air environment using 3$\omega$ method, International Journal of Thermal Sciences 64 (2013) 145–151.
[64] D. Yoon, H. Moon, Y.-W. Son, J.S. Choi, B.H. Park, Y.H. Cha, Y.D. Kim, H. Cheong, Interference effect on Raman spectrum of graphene on $SiO_2$/Si, Physical Review B 80 (12) (2009) 125422.
[65] X. Tang, S. Xu, J. Zhang, X. Wang, Five orders of magnitude reduction in energy coupling across corrugated graphene/substrate interfaces, ACS Appl Mater Interfaces 6 (4) (2014) 2809–2818.
[66] H. Zhou, C. Qiu, F. Yu, H. Yang, M. Chen, L. Hu, Y. Guo, L. Sun, Raman scattering of monolayer graphene: the temperature and oxygen doping effects, Journal of Physics D: Applied Physics 44 (18) (2011) 185404.
[67] L. Zhang, Z. Jia, L. Huang, S. O'Brien, Z. Yu, Low-temperature Raman spectroscopy of individual single-wall carbon nanotubes and single-Layer graphene, The Journal of Physical Chemistry C 112 (36) (2008) 13893–13900.
[68] M.J. Allen, J.D. Fowler, V.C. Tung, Y. Yang, B.H. Weiller, R.B. Kaner, Temperature dependent Raman spectroscopy of chemically derived graphene, Applied Physics Letters 93 (19) (2008) 193119.
[69] A.A. Balandin, Thermal properties of graphene and nanostructured carbon materials, Nature Materials 10 (8) (2011) 569–581.
[70] I. Calizo, A.A. Balandin, W. Bao, F. Miao, C.N. Lau, Temperature dependence of the Raman spectra of graphene and graphene multilayers, Nano Letters 7 (9) (2007) 2645.
[71] W. Zhao, W. Chen, Y. Yue, S. Wu, In-situ two-step Raman thermometry for thermal characterization of monolayer graphene interface material, Applied Thermal Engineering 113 (2017) 481–489.
[72] K.T. Nguyen, D. Abdula, C.-L. Tsai, M. Shim, Temperature and gate voltage dependent raman spectra of single-layer graphene, ACS Nano 5 (6) (2011) 5273–5279.
[73] W. Wang, Q. Peng, Y. Dai, Z. Qian, S. Liu, Temperature dependence of Raman spectra of graphene on copper foil substrate, Journal of Materials Science: Materials in Electronics 27 (4) (2015) 3888–3893.
[74] L.M. Malard, J. Nilsson, D.L. Mafra, D.C. Elias, J.C. Brant, F. Plentz, E.S. Alves, A.H.C. Neto, M.A. Pimenta, Electronic properties of bilayer graphene probed by Resonance Raman Scattering, Physica Status Solidi (B) 245 (10) (2008) 2060–2063.
[75] A. Compaan, H.J. Trodahl, Resonance Raman scattering in Si at elevated temperatures, Physical Review B 29 (2) (1984) 793–801.
[76] S. Périchon, V. Lysenko, B. Remaki, D. Barbier, B. Champagnon, Measurement of porous silicon thermal conductivity by micro-Raman scattering, Journal of Applied Physics 86 (8) (1999) 4700–4702.
[77] M.R. Abel, S. Graham, J.R. Serrano, S.P. Kearney, L.M. Phinney, Raman Thermometry of Polysilicon Microelectro-mechanical Systems in the Presence of an Evolving Stress, Journal of Heat Transfer 129 (3) (2006) 329–334.
[78] N. Jung, A.C. Crowther, N. Kim, P. Kim, L. Brus, Raman enhancement on graphene: adsorbed and intercalated molecular species, ACS Nano 4 (11) (2010) 7005–7013.
[79] K.F. Mak, M.Y. Sfeir, Y. Wu, C.H. Lui, J.A. Misewich, T.F. Heinz, Measurement of the Optical Conductivity of Graphene, Physical Review Letters 101 (19) (2008) 196405.
[80] R.R. Nair, P. Blake, A.N. Grigorenko, K.S. Novoselov, T.J. Booth, T. Stauber, N.M.R. Peres, A.K. Geim, Fine structure constant defines visual transparency of graphene, Science 320 (5881) (2008) 1308.
[81] A.A. Balandin, S. Ghosh, W. Bao, I. Calizo, D. Teweldebrhan, F. Miao, C.N. Lau, Superior thermal conductivity of single-Layer graphene, Nano Letters 8 (3) (2008) 902–907.
[82] Y. Yue, J. Zhang, Y. Xie, C. Wen, X. Wang, Energy coupling across low-dimensional contact interfaces at the atomic scale, International Journal of Heat & Mass Transfer 110 (2017) 827–844 Complete.
[83] J. Kim, E. Fleming, Y. Zhou, L. Shi, Comparison of four-probe thermal and thermoelectric transport measurements of thin films and nanostructures with microfabricated electro-thermal transducers, Journal of Physics D: Applied Physics 51 (10) (2018) 103002.
[84] H.D. Wang, J.H. Liu, X. Zhang, R.F. Zhang, F. Wei, Raman measurement of heat transfer in suspended individual carbon nanotube, Journal Of Nanoscience And Nanotechnology 15 (4) (2015) 2939–2943.
[85] Q. Li, J. Liu, H. Wang, X. Zhang, K. Takahashi, Optical absorptance measurement of an individual multiwall carbon nanotube using a T type thermal probe method, Review of Scientific Instruments 84 (10) (2013) 104905.
[86] J. Liu, T. Li, Y. Hu, X. Zhang, Benchmark study of the length dependent thermal conductivity of individual suspended, pristine SWCNTs, Nanoscale 9 (4) (2017) 1496–1501.
[87] H. Wang, J. Liu, X. Zhang, T. Li, R. Zhang, F. Wei, Heat transfer between an individual carbon nanotube and gas environment in a wide Knudsen number regime, Journal of Nanomaterials 2013 (2013) 3.
[88] J. Liu, Y. Hu, X. Zhang, Characterization of thermal transport and laser absorption properties of an individual graphitized carbon fiber by applying Raman thermography, Thermochimica Acta 663 (2018) 183–188.
[89] C.-M. Chen, C.-W. Hsieh, C.-F. Ho, C.-K. Sung, Insertion structures for transparent metal electrodes prepared by nanoimprint lithography, Applied Physics Express 5 (4) (2012) 044202.
[90] S. Strobel, S. Harrer, G. Penso Blanco, G. Scarpa, G. Abstreiter, P. Lugli, M. Tornow, Planar nanogap electrodes by direct nanotransfer printing, Small 5 (5) (2009) 579–582.
[91] M. Soini, I. Zardo, E. Uccelli, S. Funk, G. Koblmüller, i Fontcuberta, A. Morral, G. Abstreiter, Thermal conductivity of GaAs nanowires studied by micro-Raman spectroscopy combined with laser heating, Applied Physics Letters 97 (26) (2010) 263107.
[92] C. Yim, M. O'Brien, N. McEvoy, S. Winters, I. Mirza, J.G. Lunney, G.S. Duesberg, Investigation of the optical properties of MoS2 thin films using spectroscopic ellipsometry, Applied Physics Letters 104 (10) (2014) 103114.
[93] H. Zhang, Y. Ma, Y. Wan, X. Rong, Z. Xie, W. Wang, L. Dai, Measuring the refractive index of highly crystalline monolayer $MoS_2$ with high confidence, Scientific Reports 5 (2015) 8440.
[94] A.K. Vallabhaneni, D. Singh, H. Bao, J. Murthy, X. Ruan, Reliability of Raman

measurements of thermal conductivity of single-layer graphene due to selective electron-phonon coupling: A first-principles study, Physical Review B 93 (12) (2016) 125432.
[95] Z. Chen, W. Jang, W. Bao, C.N. Lau, C. Dames, Thermal contact resistance between graphene and silicon dioxide, Applied Physics Letters 95 (16) (2009) 161910.
[96] S. Xu, X. Wang, Across-plane thermal characterization of films based on amplitude-frequency profile in photothermal technique, AIP Advances 4 (10) (2014) 107122.
[97] S. Xu, Z. Xu, J. Starrett, C. Hayashi, X. Wang, Cross-plane thermal transport in micrometer-thick spider silk films, Polymer 55 (7) (2014) 1845–1853.
[98] X. Qian, P. Jiang, P. Yu, X. Gu, Z. Liu, R. Yang, Anisotropic thermal transport in van der Waals layered alloys $WSe_{2(1-x)}Te_{2x}$, Applied Physics Letters 112 (24) (2018) 241901.
[99] J. Zhu, D. Tang, W. Wang, J. Liu, K.W. Holub, R. Yang, Ultrafast thermoreflectance techniques for measuring thermal conductivity and interface thermal conductance of thin films, Journal of Applied Physics 108 (9) (2010) 094315.
[100] C. Zhang, W. Chen, Y. Tao, W. Zhao, S. Cai, C. Liu, Z. Ni, D. Xu, Z. Wei, J. Yang, K. Bi, Y. Chen, Electron contributions to the heat conduction across Au/graphene/Au interfaces, Carbon 115 (2017) 665–671.
[101] Q. Li, K. Katakami, T. Ikuta, M. Kohno, X. Zhang, K. Takahashi, Measurement of thermal contact resistance between individual carbon fibers using a laser-flash Raman mapping method, Carbon 141 (2013) 92–98.
[102] Q. Li, K. Xia, J. Zhang, Y. Zhang, Q. Li, K. Takahashi, X. Zhang, Measurement of specific heat and thermal conductivity of supported and suspended graphene by a comprehensive Raman optothermal method, Nanoscale 9 (30) (2017) 10784–10793.
[103] S. Sullivan, A. Vallabhaneni, I. Kholmanov, X. Ruan, J. Murthy, L. Shi, Optical generation and detection of local nonequilibrium phonons in suspended graphene, Nano Letters 17 (3) (2017) 2049–2056.
[104] Y. Zhang, A. Fan, S. Luo, H. Wang, W. Ma, X. Zhang, Suspended 2D anisotropic materials thermal diffusivity measurements using dual-wavelength flash Raman mapping method, International Journal of Heat and Mass Transfer 145 (2019) 118795.
[105] K.F. Mak, C. Lee, J. Hone, J. Shan, T.F. Heinz, Atomically Thin MoS: A New Direct-Gap Semiconductor, Physical Review Letters 105 (13) (2010) 136805.
[106] Y. Hu, A. Fan, J. Liu, H. Wang, W. Ma, X. Zhang, A dual-wavelength flash Raman method for simultaneously measuring thermal diffusivity and line thermal contact resistance of an individual supported nanowire, Thermochimica Acta 683 (2020) 178473, doi:10.1016/j.tca.2019.178473.